Modeling and Predicting Second-Harmonic Generation from Protein Molecular Structure

Bahar Asadipour, Emmanuel Beaurepaire, Xingjian Zhang, Anatole Chessel, Pierre Mahou, Willy Supatto, Marie-Claire Schanne-Klein, Chiara Stringari

Modeling and Predicting Second-Harmonic Generation from Protein Molecular Structure

Bahar Asadipour, Emmanuel Beaurepaire, Xingjian Zhang, Anatole Chessel, Pierre Mahou, Willy Supatto, Marie-Claire Schanne-Klein, and Chiara Stringari*

Laboratory for Optics and Biosciences (LOB), École Polytechnique, CNRS, Inserm, Institut Polytechnique de Paris, 91128 Palaiseau, France

(Received 2 November 2022; revised 29 September 2023; accepted 22 December 2023; published 6 March 2024)

Polarization resolved second-harmonic generation (pSHG) microscopy is increasingly used for mapping organized arrays of noncentrosymmetric proteins such as collagen, myosin, and tubulin, and holds potential for probing their molecular structure and supramolecular organization in intact tissues. However, the contrast mechanism of pSHG is complex and the development of applications in the life sciences is hampered by the lack of models accurately relating the observed pSHG signals to the underlying molecular and macromolecular organization. In this work, we establish a general multiscale numerical framework relating the micrometer-scale SHG measurements to the atomic-scale and molecular structure of the proteins under study and their supramolecular arrangement. We first develop a new method to automatically analyze pSHG signals independently of the protein type and fiber orientation. We then characterize experimentally pSHG signals in live zebrafish larvae and show that they can be used to distinguish collagen, myosin, and tubulin structures in intact tissues. We then introduce a numerical model that considers the peptide bond (PB) as the elementary SHG source in proteins and takes into account the three-dimensional (3D) distribution of PBs to predict the second-order hyperpolarizability tensor β of proteins, as well as the SHG efficiency and pSHG response of an arbitrary macromolecular assembly. We show that this model accurately reproduces pSHG measurements obtained from collagen, myosin, microtubule, and actin structures, revealing the precise dependence of SHG signals on the 3D distribution of PBs within protein assemblies. We then use our model to analyze pSHG from a 3D distribution of microtubule assemblies as a function of out-of-plane angles, angular disorder, and polarity. Finally, we demonstrate that our model predicts SHG from different molecular conformations of tubulin that are highly relevant from a biomedical point of view as associated with microtubules (de)polymerization. By bridging scales from the molecular bonds to the optical wavelength, our model provides an accurate interpretation of SHG signals in terms of protein structure and supramolecular organization.

DOI: 10.1103/PhysRevX.14.011038 Subject Areas: Biological Physics, Optics

I. INTRODUCTION

Second-harmonic generation (SHG) microscopy is a multiphoton imaging modality [1] increasingly used for label-free mapping of organized protein arrays in intact tissues [2,3]. SHG is specifically obtained from a small number of physiologically important macromolecular assemblies including fibrillar collagen [4–8], myofilaments [9–11], polarized microtubule (MT) bundles in mitotic spindles and axons [12–17], and β-amyloid plaques [18,19]. Because of its underlying physical origin and coherence properties, SHG is sensitive to the molecular structure of materials and to the spatial organization of these protein assemblies at the scale of the emitted wavelength. In particular, polarization resolved SHG (pSHG) has been shown to be sensitive to molecular order and to average 3D orientation of fibers within the focal volume [20–31]. Apart from a few attempts at superresolution imaging [32,33], the resolution of SHG is generally limited by diffraction to the micrometer dimension, i.e., ≈1000 times lower than when using cryogenic electron microscopy (CryoEM) or x-ray crystallography; therefore, pSHG microscopy probes the average organization of the harmonophores at the micron scale. Based on this readout, several structural proteins (collagen, myosin, tubulin) [21,34,35] can be detected from their pSHG response. Recent works further demonstrated the sensitivity of pSHG to protein conformational changes in myosin [11,36] and microtubules [37–39] suggesting that pSHG could become a sensitive label-free method to probe structural modifications of protein arrays in physiological conditions.

*chiara.stringari@polytechnique.edu

Moreover, SHG is sensitive to structural changes occurring during various pathological processes, potentially providing metrics relevant for both basic biomedical research and diagnostic applications [2]. This unique ability of pSHG to provide structural information in intact tissues is, however, hampered by the lack of a comprehensive model to relate the pSHG response to protein structural conformation and 3D macromolecular organization. The difficulty to develop such a quantitative model is due to the coherent nature of the SHG signal and to its dependence on molecular orientation. Indeed, several parameters govern SHG intensity in an intricate manner at different scales: (i) at the atomic scale, the nature of elementary groups that are sources of SHG ("harmonophores") within the proteins, (ii) at the molecular scale, the 3D spatial distribution of the harmonophores within the proteins, and (iii) at the optical scale (wavelength scale), the 3D macromolecular packing, organization, and density of protein assemblies. Previous efforts to elucidate the molecular source of SHG in fibrillar collagen have identified that peptide bonds (PB) between protein amino acids are likely to be the main SHG sources at the atomic scale, and that tight packing of PBs in collagen α chain results in an efficient coherent buildup of the SHG signal at the optical scale [40–43]. Using similar assumptions, we previously predicted the SHG response of myosin proteins in different conformational structures and physiological states [11].

In this work, we introduce and validate a comprehensive computational framework to model the pSHG response from an arbitrary macromolecular arrangement of proteins of known molecular structure described by the atomic positions in a Protein Data Bank (PDB) file [44]. We first show experimentally that collagen, myosin, and tubulin assemblies can be automatically identified and distinguished based on their pSHG response in a live zebrafish embryo. We then present our computational framework enabling the calculation of the second-order hyperpolarizability tensor β of a protein array from the spatial distribution of PBs at the optical scale, and the prediction of the pSHG response of an arbitrary macromolecular assembly. We show that our model is fully consistent with experimental pSHG observations and that it can be used to provide a molecular interpretation of SHG microscopy signals in terms of protein ultrastructural conformation and degree of protein organization.

II. RESULTS AND DISCUSSION

A. pSHG distinguishes different endogenous proteins experimentally

In this section we investigate experimentally whether pSHG microscopy can be used to distinguish different proteins such as collagen, myosin, and tubulin in a live organism such as a zebrafish (*Danio rerio*) larvae. For this we have modified a multiphoton microscope to perform pSHG microscopy (Appendix A 1) and developed a new method to automatically perform pSHG analysis (Appendix A 2). We first optimized the excitation and detection conditions in our custom-built pSHG microscope [see Fig. 1(a) and Appendix A 1] in order to efficiently image different protein assemblies. We chose an excitation wavelength of 1150 nm because it results in reduced scattering and endogenous intracellular multiphoton absorption compared to lower wavelengths [14,45]. We collected the SHG signals with a sensitive GaAsP photodetector placed in the forward direction path (see Appendix A 1). We adapted the excitation power to the different types of protein assemblies: collagen, myosin, and MTs. In the case of microtubules, which are significantly less efficient SHG sources [12,17] than collagen and myosin, we increased the excitation power by a factor of ≈10 to obtain a similar signal-to-noise ratio (Appendix A 1). Under these conditions, we recorded *in vivo* SHG of collagen fibers in the tail and fins [46], myosin in the skeletal muscles of the tail, and microtubule bundles in the brain and spinal cord of the zebrafish embryo [Figs. 1(b) and 1(c) herein and Fig. S1–S3 in Supplemental Material [47]]. The SHG efficiencies for the three proteins in zebrafish embryos show that collagen is the most efficient while microtubules are the least efficient [Fig. 1]. We attribute the SHG intensity heterogeneity within the images [Fig. 1(c)] and the large distribution at the pixel base [Fig. 1] to different protein densities and 3D packing in different regions of the tissue.

As depicted in Fig. 1(a), we used a rotating half-wave plate located before the excitation objective to control the incident polarization in the sample plane yz (Appendix A 1) and collect pSHG responses. As expected, SHG intensity depends on the incident polarization angle φ, and the shape of the polarimetric response is specific to each protein assembly [Figs. 1(c) and 1(d)]. To quantify the pSHG responses within the images, we first determined the relative angle of the maximum (highest minimum) SHG intensity with respect to the fiber axis for one-peaked (two-peaked) pSHG profiles [see Appendix A 2 and Fig. 1(e)], which results to be ≈0° for collagen and microtubules (larger SHG signal parallel to the fiber axis than perpendicular to it) and ≈90° for myosin (larger SHG signal perpendicular to the fiber axis). According to the relative angle, we then fitted the curves in a region of interest (ROI) with Eq. (A21) in Appendix A 10 that is valid for cylindrical symmetry. At the pixel level, we implemented a fully automated image analysis method based on structure tensor analysis [48] and FFT to detect fiber direction and calculate the values of the pSHG anisotropy factor γ in each pixel of the image, independently of the protein type and fiber orientation (Appendix A 2 and Figs. S1, S2g, and S3f in Supplemental Material [47]). The anisotropy factor γ was thus extracted from both the fits of ROI [Table IV and Fig. 1(d)] and the FFT-based analysis at the pixel level automated single pixel analysis [Fig. 1(f) herein and

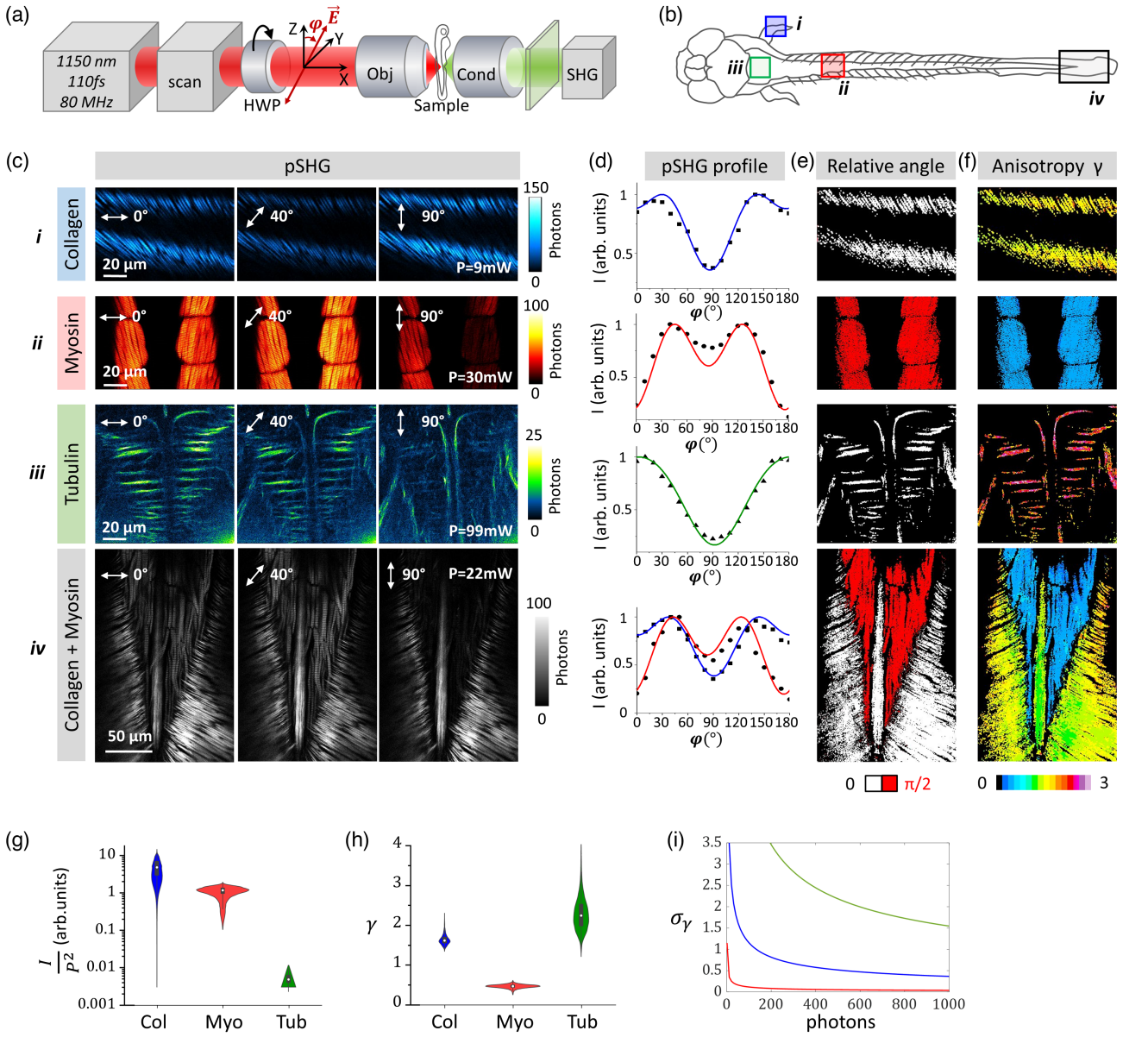

FIG. 1. Polarization resolved SHG (pSHG) measurements on different fibrillar structures in a live zebrafish larva at 5 days post fertilization (dpf). (a) pSHG microscopy setup. A rotating half-wave plate (HWP) is installed before the objective and is used to control the direction of the incident linear polarization in the yz imaging plane of the laboratory system. (b) Scheme of a zebrafish larva at 5 dpf. Collagen and myosin signals are observed in the pectoral fins (i) and in the trunks (ii), while tubulin signals are observed in the brain and spinal cord (iii). (c) pSHG images recorded at polarization angles $\varphi = 0°$, 40°, and 90° as indicated by the arrows. pSHG raw data are displayed in Movies M1–M4 in Supplemental Material [47]. (d) Dependence of the SHG intensity in a region of interest as a function of the incident polarization angle $\varphi - \varphi_0$, where φ_0 is the angle of the protein fiber axis. Curves are obtained by the least square fitting of Eq. (A21) (see Table IV). (e) Maps of the relative angle of the maximum (highest minimum) SHG intensity with respect to the fiber axis for one-peaked (two-peaked) pSHG profiles extracted automatically with the structure-tensor analysis and FFT-based analysis (Appendix A 2). (f) Maps of the anisotropy factor γ for the three proteins calculated with the FFT-based analysis (Appendix A 2) taking in account the relative angle of the maximum (highest minimum) SHG intensity. pSHG distinguishes myosin and collagen within the same image based on the anisotropy factor. 3D stack of the SHG intensity, relative angle, and anisotropy factor of the region containing both collagen and myosin are displayed in Movies M12–M14, respectively [47]. (g),(h) Pixel distribution of the total SHG intensity normalized by the square of the incident power (g) and anisotropy factor, calculated with the FFT-based analysis (h) in the three proteins of the zebrafish embryo. (i) Theoretical standard deviation σ_γ of the anisotropy factor γ as a function of the number of photons for the three types of structures: collagen (blue, $\gamma = 1.5$), myosin (red, $\gamma = 0.5$), and microtubules (green, $\gamma = 2.5$).

Figs. S1–S3 [47]]. γ is expected to provide the ratio of the two independent components of the second-order susceptibility tensor χ_{zzz} and χ_{zxx} in the cylindrical symmetry approximation [Eq. (A25) in Appendix A 10].

The γ anisotropy factors measured here in live embryos are consistent with measurements previously reported in literature in various proteins: γ has been measured in the range between 0.8 and 1.8 for collagen [20–22,25], between 0.3 and 0.7 for myosin [11,21], and between 1.7 and 3.3 for microtubules [37–39].

Based on the anisotropy factor γ, we find that pSHG can distinguish between different sources of SHG at the pixel scale [Figs. 1(f) and 1(h)], within the same image in 2D [Figs. 1(d) and 1(f) last row] and in 3D structures (Movies M12, M13, and M14 in Supplemental Material [47]) provided that the signal-to-noise ratio is sufficient. For example, a total number of photons over the all incident polarization between 300 and 1000 per pixel is enough to measure the different values of γ of different proteins, collagen, myosin, and tubulin [Figs. 1(f) and 1(h) and Table III], and therefore to distinguish them ($\gamma_{\text{tubulin}} - \gamma_{\text{collagen}} \approx 1$, $\gamma_{\text{collagen}} - \gamma_{\text{myosin}} \approx 1$, $\gamma_{\text{tubulin}} - \gamma_{\text{myosin}} \approx 2$). This is in agreement with the theoretical calculation [49,50] of the standard deviation of γ [$\sigma_\gamma(N_{\text{photons}})$] as a function of the number of photons [Fig. 1(i) and Figs. S4a and S4b]. To distinguish instead γ variations close to $\approx$0.2, that correspond to different protein conformations [11,36,38,39], less than 50 photons are necessary for myosin (Fig. S4c [47]) while $\approx 60 \times 10^3$ photons are necessary for tubulin assemblies (Fig. S4d [47]). The low microtubules SHG efficiency [Fig. 1(g)] and the larger number of photons required to distinguish between different tubulin conformations (Fig. S4d [47]) makes pSHG experimentally more challenging in microtubules than in collagen and myosin. Our experiments, combined with our automated image analysis method, demonstrate that pSHG profiles and the anisotropy factor γ can be used to discriminate between the proteins collagen, myosin, and microtubule, providing automated identification of these proteins in tissues in a label-free and noninvasive way.

B. Modeling SHG response of proteins from peptide bonds distribution

We develop a comprehensive numerical model that takes into account the molecular structure of any protein to accurately describe its pSHG response. Theoretical approaches previously modeled the collagen hyperpolarizability by using quantum chemical calculations on building blocks and additive model [51–53]. A simplified model often used in the literature [10,21,25,37,38] relates the anisotropy factor γ of proteins with complex 3D structures to the average polar angle ψ of the SHG elementary sources (or harmonophores) with respect to the fiber axis [Eq. (A27) in Appendix A 12]. This approximation is adequate for protein assemblies where harmonophores alignment is present at multiple scales, such as in collagen fibers. In fact in this case, the average polar angle measured by pSHG is close to the pitch angle of the helices measured by x-ray diffraction [21,25,26]. However, this model is too simple to analyze the case of more complex assemblies characterized by a broad angular distribution of proteins at the optical level, or made of proteins where the secondary structures (α helix and β sheet) are less aligned at the molecular scale, such as in tubulin. Indeed in that case, the SHG intensity and the anisotropy factor are expected to depend at the same time on the average orientation, the angular distribution, and the polarity of the elementary harmonophores in the excitation volume.

To decipher the relationship between protein hyperpolarizability and protein structure, we first identified the elementary source of SHG within proteins, we used a unique tensor component to describe its SHG response, without any quantum calculation, and we then calculated the protein hyperpolarizability β from its molecular structure in a bottom-up manner. Molecules with π-electron donors and acceptors with partial charge transfer between the two groups are a source of nonlinear optical susceptibility [54]. Previous studies using sum-frequency vibrational spectroscopy [55], hyper-Rayleigh scattering (HRS) [42,43], SHG measurements [40], and theoretical calculations [51] have determined that the primary molecular origin of SHG in collagen is the delocalization of the π electron between the -C = O and the -N-H of the PB [Fig. 2(a)].

We built a bottom-up model to predict the second-order hyperpolarizability tensor and the pSHG response of any protein, taking into account its molecular structure [Fig. 2(b)], using the following assumptions.

(i) We assumed that the elementary source of SHG is located in the PB independently of amino acid residue along the protein chain (see Appendix A 6). We assumed that the amide group -NH-CO-, which composes the backbone of the protein structure, has a preferred hyperpolarizability axis along the C-N PB between the amino acids of the proteins (z') [Fig. 2(a)]; hence we considered only the hyperpolarizability tensor component $\beta_{z'z'z'}$ of the PB. Thus we neglected all its other hyperpolarizability tensor components, relying on previous quantum chemistry calculations that showed that they are typically at least a factor of 3 smaller in magnitude [41]. The impact of this approximation will be discussed in Sec. II C.

(ii) We made the assumption of a weak coupling between the SHG harmonophores along the PB within the protein, which allows us to calculate the bulk second-order hyperpolarizability tensor by coherent summation of all the individual SHG emitters weighted by their orientations, as already assumed by other theoretical studies [40–42,51,53,60]. Of note, assumptions (i) and (ii) neglect the possible contribution

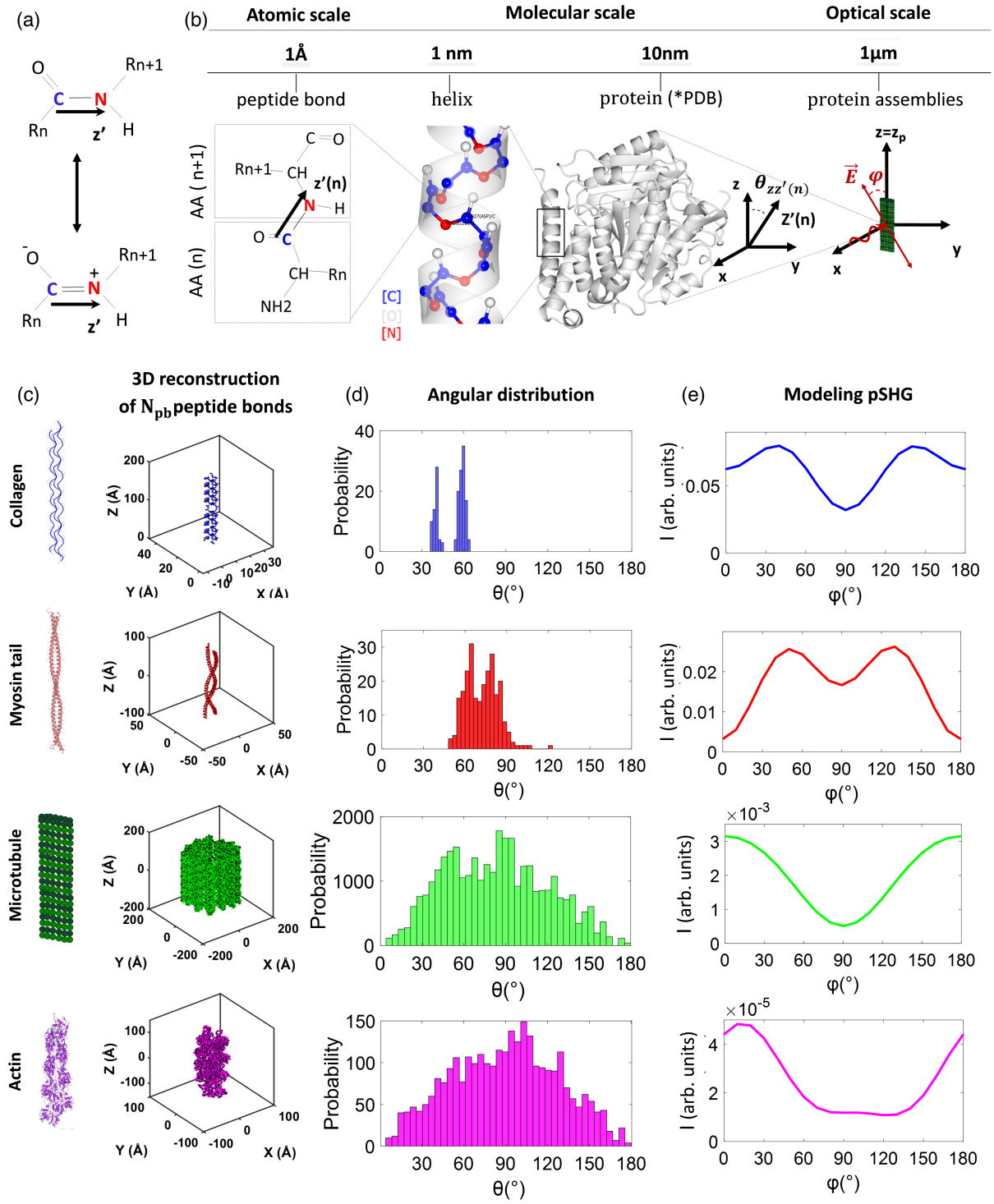

FIG. 2. Modeling pSHG from protein peptide bonds distribution. (a) Peptide bond (C—N) π orbitals represented by their two resonance forms with a preferred hyperpolarizability axis along z'. (b) Multiscale distribution of peptide bonds between amino acids (AA) at the atomic scale (Å), molecular scale in helix (nm) and protein (10 nm), and at the optical scale in protein assemblies (µm). The $z'(n)$ axis along the peptide bond n between the AA (n) and the AA ($n+1$) is defined in the xyz laboratory system by the angle $\theta_{zz'(i)}$. The protein axis z_p is aligned along the z laboratory axis. (c) Three-dimensional reconstruction of the peptide bonds distribution of proteins from their molecular structure extracted from PDB files: collagen triple helix [56], myosin tail [57], reconstructed microtubule in GTP-tubulin state [58], and actin filament [59]. Nitrogen atoms are represented by black dots, while carbon atoms are represented by colored dots and the PBs by colored lines. 3D reconstructions are displayed in Movies M7–M11 [47]. All the proteins are lying in the imaging plane yz and their axis z_p is aligned with the laboratory z axis. (d) Distribution of $\theta_{zz'}$ angles between the peptide bond axis z' and the laboratory z axis. (e) Simulated SHG intensity per number of peptide bonds as a function of the polarization incident angle φ.

TABLE I. Modeling different proteins.

Protein	I_{PB} [a]	β_{PB}^{eff}	$\gamma = \sqrt{\frac{I(\varphi_0)}{I(\varphi_0+90°)}}$	$\frac{\beta_{zzz}}{\beta_{zxx}}$	$\bar{\theta}_{zz'}$ [b]	$SD(\theta_{zz'})$	DCS
Collagen	0.062	0.25	1.40	1.41	52°	9°	0.07
Myosin tail	0.017	0.130	0.44	0.49	72°	12°	0.15
Tubulin dimer (GTP-tubulin)	0.003	0.056	1.48	3.70	83°	37°	4.33
Microtubule (GTP-tubulin)	0.002	0.044	2.49	2.49	83°	37°	0.01
Actin	2.4×10^{-5}	0.005	1.93	−3.9	90°	38°	3.78

[a]The simulated average SHG intensity per PB (I_{PB}), the effective protein hyperpolarizability per PB (β_{PB}^{eff}), the anisotropy factor γ, the ratio of the hyperpolarizability tensor components and deviation from the cylindrical symmetry (DCS) are calculated as described in Appendix A 10.

[b]The average $\bar{\theta}_{zz'}$ and the standard deviation $SD(\theta_{zz'})$ of the angular distribution of the PBs are extracted from the molecules structure of the proteins as described in Appendix A 6.

of aromatic amino acids (His, Phe, Trp, Tyr) [41,61]. We expect that these assumptions may impact the modeling of proteins containing a non-negligible number of aromatic amino acids such as tubulin. For collagen triple helix and myosin tail we do not expect deviation from the model as there are no aromatic amino acids. Introducing the contribution of the aromatic amino acids would require a more advanced modeling that is beyond the scope of this paper [61,62]. The relevance of this approximation will be further commented on in Sec. III.

(iii) Since protein lengths (≈10 nm) are negligible compared to the optical wavelength (≈1 μm) we did not take into account the retardation of the exciting field and the harmonic field along proteins.

(iv) We considered the case of plane-wave excitation and neglected the effect of the Gouy phase shift of strongly focused beams, which was shown to have only a limited effect on measured second-harmonic tensorial responses [63]. The impact of this approximation will be evaluated in Sec. II C and in Supplemental Material B [47].

(v) Finally, we neglect the effect of birefringence, diattenuation, and depolarization due to scattering of the excitation beam, as well as polarization scrambling upon scattering of the harmonic signal that occurs in thick anisotropic tissues and depends both on the scattering coefficients and on imaging depth [30,63–66]. The impact of this approximation will be discussed in Secs. II C and III.

We considered the structures of the following proteins: collagen triple helix, myosin α-helical coiled-coil tail, tubulin dimer (GTP-tubulin), microtubule in different molecular conformations (GTP-tubulin, GDP-tubulin, and taxol-bound tubulin), and actin (Table V and Appendix A 6). We note that, as the myosin tail dominates the pSHG response of the entire myosin molecule in terms of both PB number and organization [11], for simplicity we do not consider here the myosin head. For each case, we first extracted the locations and the orientations of all the PBs between amino acids from the atomic coordinates of the protein of interest in the Protein Data Bank [44] [Fig. 2(b) and Appendix A 6]. We reconstructed the three-dimensional distribution of PBs [Fig. 2(c) herein and Figs. S5 and S6, and Movies M7–M11 in Supplemental Material [47]], plotted the distribution of the polar angles $\theta_{zz'}$ of the harmonophores [Fig. 2(d)], and measured the average $\bar{\theta}_{zz'}$ and the standard deviation $SD(\theta_{zz'})$ of the angular distribution (Table I). Second, considering a coherent summation of the responses of all individual PBs in the protein [Eq. (A8)], we calculated all the components of the second-order hyperpolarizability tensor β_{PB} normalized to the number of PBs [Eqs. (A10)–(A16) in Appendix A 9]. Finally, we simulated the pSHG signal as a function of the polarization incident angle φ using the β_{ijk} components, both for the general case [Eq. (A20)] and in the case of cylindrical symmetry [Eq. (A21)] [see Appendix A 10, Fig. 2(e) herein, and Figs. S7 in Ref. [47]]. We used the following metrics to describe the SHG responses of every protein: the simulated average SHG intensity per PB (I_{PB}), the effective protein hyperpolarizability per PB (β_{PB}^{eff}), the anisotropy factor γ calculated as the ratio of the SHG intensities along and perpendicular to the protein main axis, and the ratio of the two hyperpolarizability tensor components β_{zzz}/β_{zxx} using Eqs. (A22)–(A25), respectively (see Appendix A 10). The two latter metrics γ and β_{zzz}/β_{zxx} aim to quantify the validity of the cylindrical symmetry in every protein of interest because they provide similar results only if the cylindrical symmetry is valid. For the same purpose, we defined the deviation from the cylindrical symmetry (DCS) with Eq. (A26) (see Fig. S7d [47]).

C. Peptide bond SHG model reproduces experimental results

We first confirmed that the characteristic shapes of the pSHG profiles predicted from the PDB protein structures [Figs. 2(e) and 3(a)] are similar to the experimental shapes [Fig. 1(d)] for all proteins. The simulated pSHG profile per PB has different amplitudes for the different proteins considered [Fig. 3(a)], and therefore the computed average SHG intensity per PB (I_{PB}) has different magnitudes

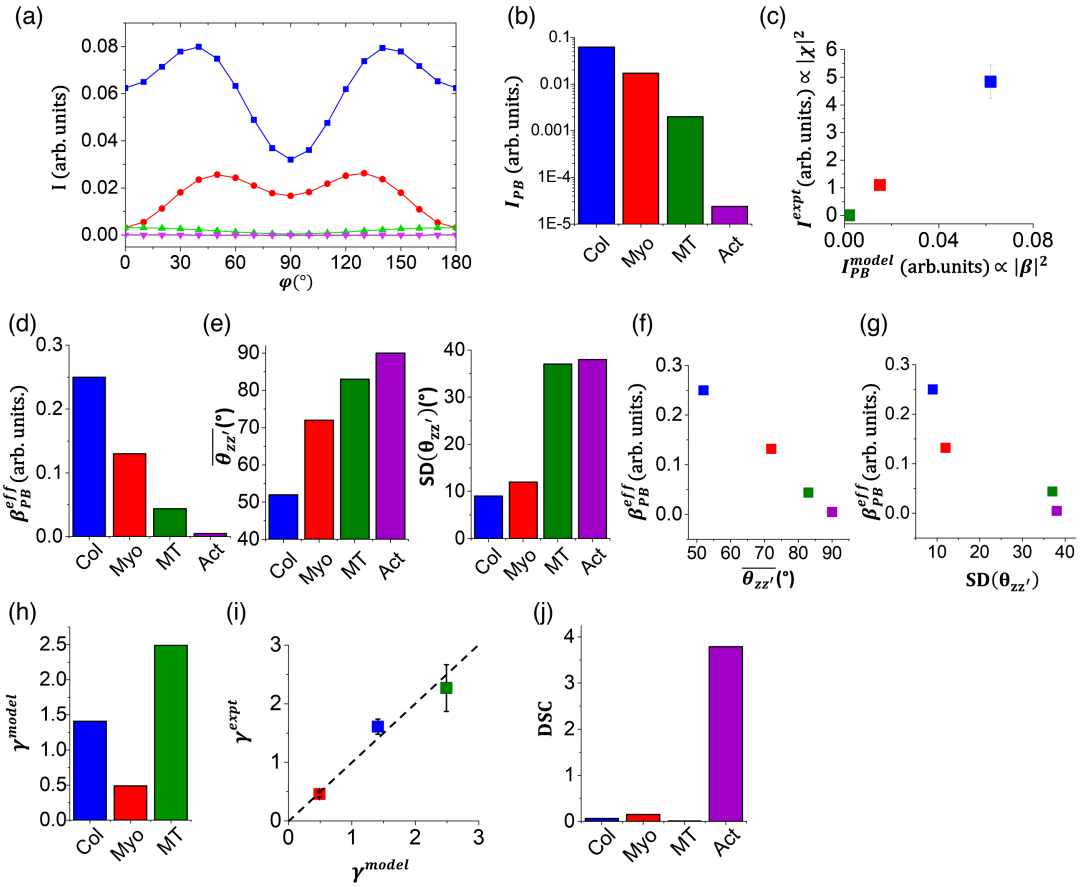

FIG. 3. Modeling pSHG from the peptide bond distribution is consistent with experimental observations. (a) Simulated SHG intensity per number of peptide bonds as a function of the polarization incident angle φ in collagen (blue squares), myosin tail (red circles), microtubule (green triangles), and actin (magenta triangles) filaments. (b) Modeled average SHG intensity per peptide bond averaged over all the incident polarization angles φ. (c) Comparison between the experimental SHG intensities normalized by the square of the incident power and the modeled SHG intensity per PB (I_{PB}). (d) Modeled effective protein hyperpolarizability per PB (β_{PB}^{eff}). (e) Average and standard deviation of the $\theta_{zz'}$ PB polar angle distribution. (f),(g) Effective protein hyperpolarizability per PB as a function of the average (f) and standard deviation of the $\theta_{zz'}$ PB polar angle distribution (g). (h) Modeled anisotropy factor γ. (i) Comparison between the experimental anisotropy factor and the modeled anisotropy factor γ. (j) Deviation from cylindrical symmetry (DCS).

[Table I and Fig. 3(b)]. I_{PB} accurately accounts for experimental SHG measurements in collagen, myosin, and microtubules [Fig. 3(c)]. While collagen has the highest SHG efficiency per PB, microtubules total SHG intensity is predicted to be 2 orders of magnitude smaller [Figs. 3(a) and 3(b)], in agreement with experiments [Fig. 1(g) and previous literature [12,17]]. The calculations also predict that SHG efficiency per PB is 4 orders of magnitude smaller for actin than for myosin, consistent with experimental evidence that actin filaments do not efficiently produce SHG, while myofilaments do [10,67].

We note that the computed average SHG intensity per PB (I_{PB}) is calculated only from the molecular hyperpolarizability (β) of the proteins (Appendix A 8), without any consideration of density or macromolecular organization. In contrast, the experimental SHG measurements at optical scale in tissues are determined by the bulk response of the tissue, the so-called susceptibility tensor $\chi^{(2)}$, that depends not only on the molecular hyperpolarizability but also on the organization and the degree of alignment of the protein assemblies at the optical scale as well as on their density inside the focal volume [Eq. (A2)]. Indeed, the effective susceptibility χ^{eff} of a tissue is calculated by multiplying the effective protein hyperpolarizability per PB ($\beta_{\text{PB}}^{\text{eff}}$) with the density of PBs, i.e., the number of PBs per volume (V): $\chi^{\text{eff}} = N_{\text{PB}} \times \beta_{\text{PB}}^{\text{eff}}/\epsilon_0 V$, in the basic case of proteins aligned within the imaging plane (see Sec. II D for more complex protein assemblies). While this explains the heterogeneous SHG intensity in the tissues [Figs. 1(c) and 1(g)], we nevertheless find similar orders of magnitude between proteins [Fig. 3(c)].

We then evaluated the effective hyperpolarizability per PB $\beta_{\text{PB}}^{\text{eff}}$ [Eq. (A23)] for the different proteins [Table I and Fig. 3(d)] and analyzed how it relates to the distribution of

the PBs inside the protein [Fig. 3(e)]. In particular, we found that $\beta_{\mathrm{PB}}^{\mathrm{eff}}$ is anticorrelated with the mean value of the PB polar angles $\bar{\theta}_{zz'}$ [Table 1 and Fig. 3(f)]. For example, the collagen protein is characterized by $\bar{\theta}_{zz'} = 52°$ and exhibits a large effective hyperpolarizability, while microtubules are characterized by $\bar{\theta}_{zz'} = 83°$, and have a one order of magnitude smaller effective hyperpolarizability [Figs. 3(d), 3(e), and 3(f)]. Actin is characterized by $\bar{\theta}_{zz'} = 90°$, and has an effective hyperpolarizability 2 orders of magnitude smaller than collagen. This is consistent with the fact that centrosymmetric distributions of PBs (with $\bar{\theta}_{zz'} = 90°$) cannot act as efficient sources of SHG. Along the same line, we also observed that there is an anticorrelation of the protein effective hyperpolarizability with the standard deviation of the angular distribution of PBs $\mathrm{SD}(\theta_{zz'})$ [Fig. 3(g)]. In general, structures with limited PB angular dispersion such as collagen triple helix and myosin α-helical coiled-coil tail have a higher effective hyperpolarizability than structures with large PB angular dispersion such as microtubules [Figs. 3(d), 3(e), and 3(g)].

To further validate our model, we estimated the absolute value of the effective hyperpolarizability for proteins of known length by multiplying the computed effective protein hyperpolarizability per peptide bond $\beta_{\mathrm{PB}}^{\mathrm{eff}}$ by the number of peptide bonds and by the previously estimated [43] hyperpolarizability of the peptide bond $\beta_{z'z'z'} = 0.67 \times 10^{-30}$ esu (see Appendix A 13). For a $[(\mathrm{Pro\text{-}Pro\text{-}Gly})_{10}]_3$ collagenlike polypeptide whose size is negligible compared to the optical wavelength, our model predicts a value of $\beta_{\mathrm{PB}}^{\mathrm{eff}} = 14.6 \times 10^{-30}$ esu, consistent with experimental values previously reported using HRS [42] (Table VIII).

Finally, we evaluated the anisotropy factor γ [Eq. (A24)] for the different proteins considered [Fig. 3(h)]: we calculated $\gamma = 1.4$ for collagen, 0.44 for myosin tail, and 2.49 for microtubules (GTP-tubulin), in good agreement with our experimental measurements [Figs. 1(d), 1(f), and 3(i)] and with values reported in literature [10,11,20,21,24–26,28,36–38]. The modeled γ for myosin tail is in agreement with the modeled values for the entire myosin molecule in resting state [11] as well as with experimental measurements in resting state [11,36]. For collagen protein, we found that the hyperpolarizability tensor component β_{zzz} is significantly larger in magnitude than the other contributing tensor component ($\beta_{zzz} > \beta_{zxx}$) [Eq. (A10)], in agreement with previous theoretical modeling (Table SI in Supplemental Material A [47]) [51–53].

To estimate the impact of the assumption of unique hyperpolarizability tensor component $\beta_{z'z'z'}$ for the elementary harmonophore PB, we considered also the second biggest component of the tensor, by introducing a perpendicular dipole in the plane of the amide group (≈3 times smaller than the PB dipole as estimated in Ref. [41]), and we obtained only a slight variation (≈15%–20%) in the γ value of collagen. We note that modeling the tensor with one unique hyperpolarizability component $\beta_{z'z'z'}$ gives in collagen the best agreement with the experimental values [Figs. 1(f) and 1(h) and Refs. [10,20,21,24–26]] and is in perfect agreement with the quantum mechanical calculations by Tuer *et al.* [51]. Other previous theoretical modeling in collagen, that considers all the components of the amide tensor [53] and uses a nonlinear optical prediction and data analysis plugin (NLOPREDICT) [68], obtained different values of the anisotropy factor of collagen depending on the quantum chemical calculation method used (see Supplemental Material A [47] and Table SI). We also note that, by assuming a unique hyperpolarizability tensor component of the elementary harmonophore, we cannot account for the chiral-specific SHG of proteins. However, as chiral-specific SHG is typically ≈10 times smaller than the achiral SHG [69], we expect that neglecting all the other tensor components would not significantly affect the calculations. On the other hand, modeling of chiral-specific SHG would require us to consider the magnetic dipolar response of the elementary harmonophore, which is beyond the scope of this paper [69].

We also evaluated the relevance of the cylindrical symmetry approximation. For collagen, myosin tail, and microtubules, the computed pSHG profiles [Fig. 2(e) herein and Fig. S7b, Ref. [47]] show good resemblance with the cylindrical symmetry pSHG profiles (Fig. S7c), resulting in low values of DCS [Fig. 3(j)] and a good agreement between γ calculated with the SHG intensities [Eq. (A24)] and β_{zzz}/β_{zxx} [Eq. (A25)] calculated with the hyperpolarizability tensor components (Table I). In contrast, for tubulin dimer (Fig. S5d) and actin filament (Fig. S7) there is a discrepancy between the pSHG profiles for the general case and the cylindrical symmetry assumption (Fig. S7), resulting in high values of DCS and a big difference between γ and β_{zzz}/β_{zxx} values (Table I). We note that, while tubulin dimers do not have cylindrical symmetry themselves, the cylindrical symmetry of microtubules derives from the arrangement of tubulin dimers in 13 protofilaments assembled around a hollow core [70]. We further confirmed that for structures with low DCS (collagen, myosin, and microtubules), for which the cylindrical symmetry is valid, the computed β_{zzz}/β_{zxx} values are in agreement with the values fitted with Eq. (A21) assuming cylindrical symmetry (Table VI).

We estimated the impact of the plane-wave approximation in the calculation of the anisotropy factor (see Supplemental Material B [47]). We first estimated the electric field depolarization induced by a high numerical aperture objective used in our experimental work (NA = 1.04). We found that the axially polarized (x-polarized) electric field component has a maximum intensity of approximately 30% of the maximum of the polarized component in the imaging plane (z polarized). The values of the anisotropy factor calculated without the plane wave (see Table SII in Supplemental

Material B) slightly differ from the ones with a plane wave, but they are still in good agreement with the experimental values measured in our paper (Figs. 1 and 3) and in previous literature [11,20–22,25,37–39].

We point out that the anisotropy factor γ in anisotropic thick tissues can also be affected by diattenuation or, to a lesser extent, birefringence experienced by the incident excitation in depth [30,63–65,71]. Nevertheless, previous numerical simulations and experiments in rat-tail tendon showed that birefringence and related effects do not affect significantly the value of the anisotropy factor at depths smaller than 40 m [63,64], while pSHG imaging experiments in collagen and myosin were performed in this work at 20 m depths (Table III). Strong diattenuation of the incident laser can affect the anisotropy factor γ, as observed in rat-tail tendon, because of much stronger scattering for polarization perpendicular to the fibers' direction than parallel to them. However, we image here in tissues with modest diattenuation ratio, as the scattering coefficient of the brain of zebrafish embryo at 5 days post fertilization (dpf) is moderate, since it is constituted mainly by cell bodies. Moreover, the excitation wavelength of 1150 nm used in this work strongly reduces scattering, so that attenuation is strongly reduced and diattenuation is thus negligible. It explains why the values of the anisotropy factor modeled here (Table I), neglecting both birefringence and depolarization, are in good agreement with the experimental values measured in zebrafish [Figs. 1(d), 1(f), and 3(i)].

A simplified model is often used in literature [10,21,25,37,38], using a single polar angle ψ of the harmonophores with respect to the fiber axis [Eq. (A27) in Appendix A 12]. We point out that such a model is appropriate only for the case of collagen where the PB distribution is narrow and ψ is equivalent to the average $\bar{\theta}_{zz'}$ of the PB polar angle distribution [Fig. 2(d) and Table VII in Appendix A 12], resulting in a correct prediction of the effective hyperpolarizability per PB (Table VII). For structures where the PB angular distribution is broader, such as myosin and microtubules, however, the simplified model fails to describe the actual PB distribution [Fig. 2(d) and Table VII] and to estimate the effective hyperpolarizability per PB $\beta_{\mathrm{PB}}^{\mathrm{eff}}$ (Table VII). As the angular distribution of the harmonophores in the protein broadens, the discrepancy between the two models increases (Table VII), illustrating the need to use our more comprehensive approach to properly account for the complex dependence of the protein hyperpolarizability tensor β on the 3D angular distribution of PBs within the protein.

D. Modeling 3D protein assemblies

To further demonstrate the potential of our model, we predicted the SHG signals at the optical scale depending on protein spatial organization using microtubule assemblies as an example. The SHG bulk properties $\chi^{(2)}$ of tissues are determined both by the values of the molecular hyperpolarizabilities of proteins β as well as by the organization and the degree of alignment of the SHG protein assemblies at the optical scale [Eq. (A2)]. The critical parameters that modulate SHG signals and the bulk $\chi^{(2)}$ in tissues are thus the protein density, the orientation of the proteins with respect to the optical axis, the orientation distribution of the proteins, and the polarity within the focal volume. We considered the following microtubules assemblies (Fig. 4): (i) microtubules lying out of the imaging plane zy, with different out-of-plane angles α [Fig. 4(a)], (ii) microtubule assemblies with various amounts of angular dispersion δ out of the imaging plane [Fig. 4(b)], and (iii) microtubule assemblies with different polarities [Fig. 4(c)].

Our calculations indicate that increasing the out-of-plane angle α results in a decrease in pSHG modulation [Fig. 4(d)] and in total SHG intensity with a minimum at $\alpha = 90°$ when the microtubule is aligned along the laser propagation axis x. The β_{zzz}/β_{zxx} ratio calculated with the hyperpolarizability tensors components increases with α, similar to the case of collagen in a previous publication [72] while γ calculated with SHG intensities decreases with α [Fig. 4(e)]. DCS increases with α with a maximum at $\alpha = 90°$ [Fig. 4(e)]. We note that $\gamma = (\beta_{zzz}/\beta_{zxx})$ only in the case of cylindrical symmetry when the microtubule lies in the imaging plane yz, while the difference between γ and β_{zzz}/β_{zxx} increases with DCS [Fig. 4(e)]. Increasing the angular dispersion angle δ of the microtubule distribution also causes a decrease in SHG intensity and pSHG modulation [Figs. 4(f) and 4(g)]. The predicted increase of β_{zzz}/β_{zxx} with δ [Fig. 4(g)] is also similar to previous calculations in collagen [23,25,63]. We predicted a smaller decrease of γ with α and we observed that the discrepancy between β_{zzz}/β_{zxx} and γ goes along with an increase of DCS [Fig. 4(g)]. Finally, the simulation of microtubule assemblies with different polarities [Fig. 4(h)] predicts a quadratic dependence of the SHG intensity on the number of microtubules with the same polarity [Fig. 4(i)]. Maximum SHG is expected when all microtubules have the same polarity such as in axons, and minimum SHG is expected from microtubule assemblies with mixed polarity such as in dendrites, as experimentally observed [16,17,73].

E. Modeling microtubules with different tubulin molecular conformations

To further demonstrate the potential of our modeling and its sensitivity to protein ultrastructure, we modeled and predicted pSHG signal in microtubules with different tubulin molecular conformations that are highly relevant from a biomedical point of view. This section is based on published tubulin structural information [58] combined with our predictive modeling. Microtubules are essential for cell morphology, intracellular transport, and cell division. Microtubule network is highly dynamic and its

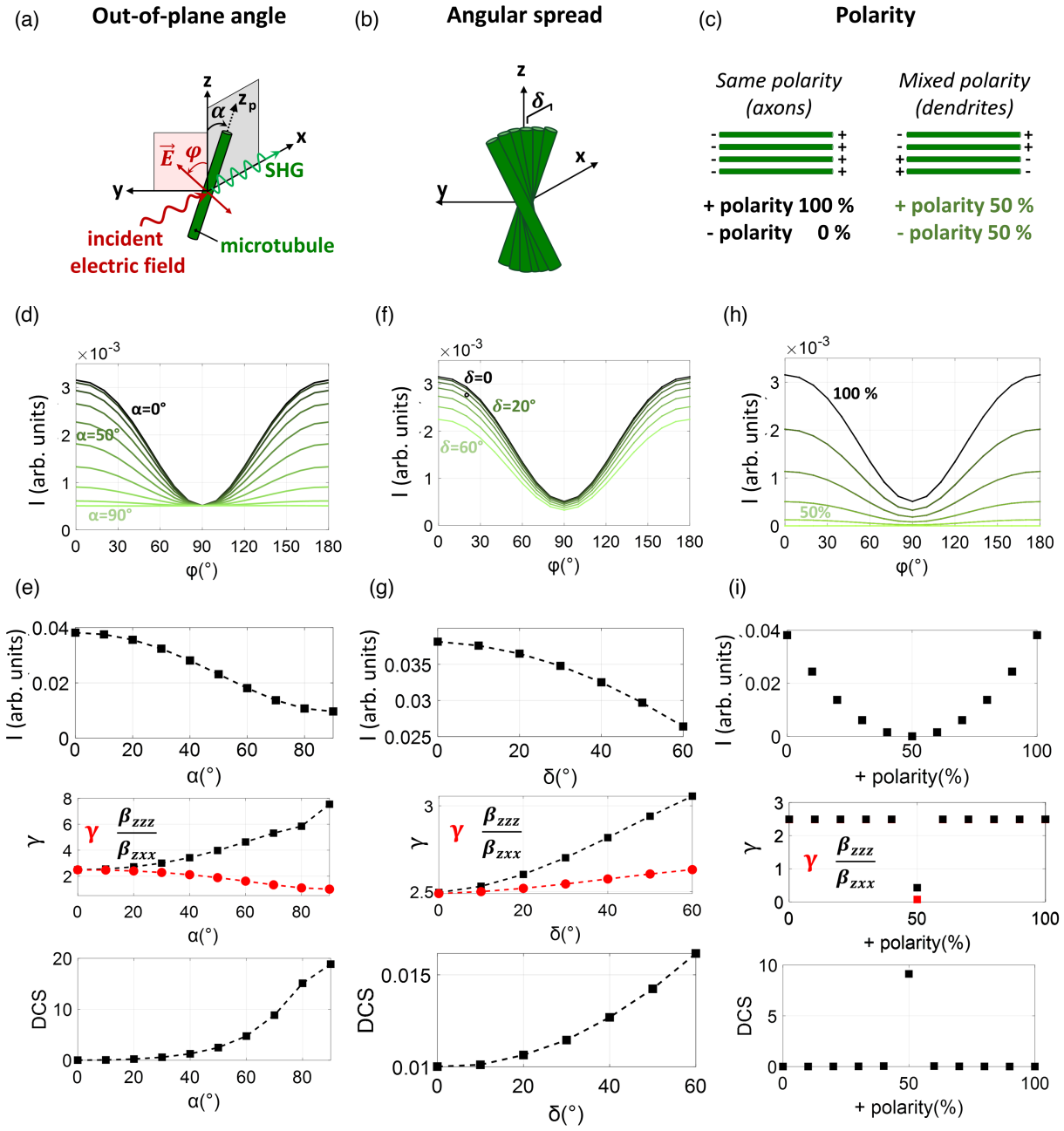

FIG. 4. Modeling pSHG intensity in a 3D macromolecular distribution of microtubules (a) schematic a microtubule tilted out of the yz imaging plane by an angle α. (b) Schematic of a microtubule distribution with angular spread δ. (c) Distribution of microtubules with the same polarity and with opposite polarity. (d)–(h) Calculated SHG intensity per peptide bond as a function of the polarization incident angle φ for different out-of-plane angles α (d), different values of the microtubules angular spread δ (f), and percentage of microtubules with the same polarity (h). (e)–(i) Calculations of SHG intensity per PB I_{PB}, anisotropy factor γ (red circles), the ratio (black squares) of the hyperpolarizability tensor components β_{zzz} and β_{zxx} and deviation from cylindrical symmetry as a function of the microtubules out-of-plane angle α (e), angular spread δ (g), and polarity (i).

dynamic instability is regulated by the biochemical transition of single tubulin dimers defined by GTP hydrolysis. When bound to GTP the tubulin dimer is stable while GDP-bound conformation is unstable and prone to depolymerization [74]. Anticancer agents like taxol stabilize microtubule network by increasing the GTP-bound tubulin dimer conformation, therefore suppressing microtubule dynamics, blocking mitosis and tumor cell proliferation [75,76]. The tight connection between tubulin ultrastructure [58] and microtubule polymerization state and hence the stability of the microtubule lattice is thus highly relevant to cancer [76] as well as to many neurodegenerative diseases [77,78]. Here we performed simulations of microtubule in different molecular conformations (GDP-tubulin,

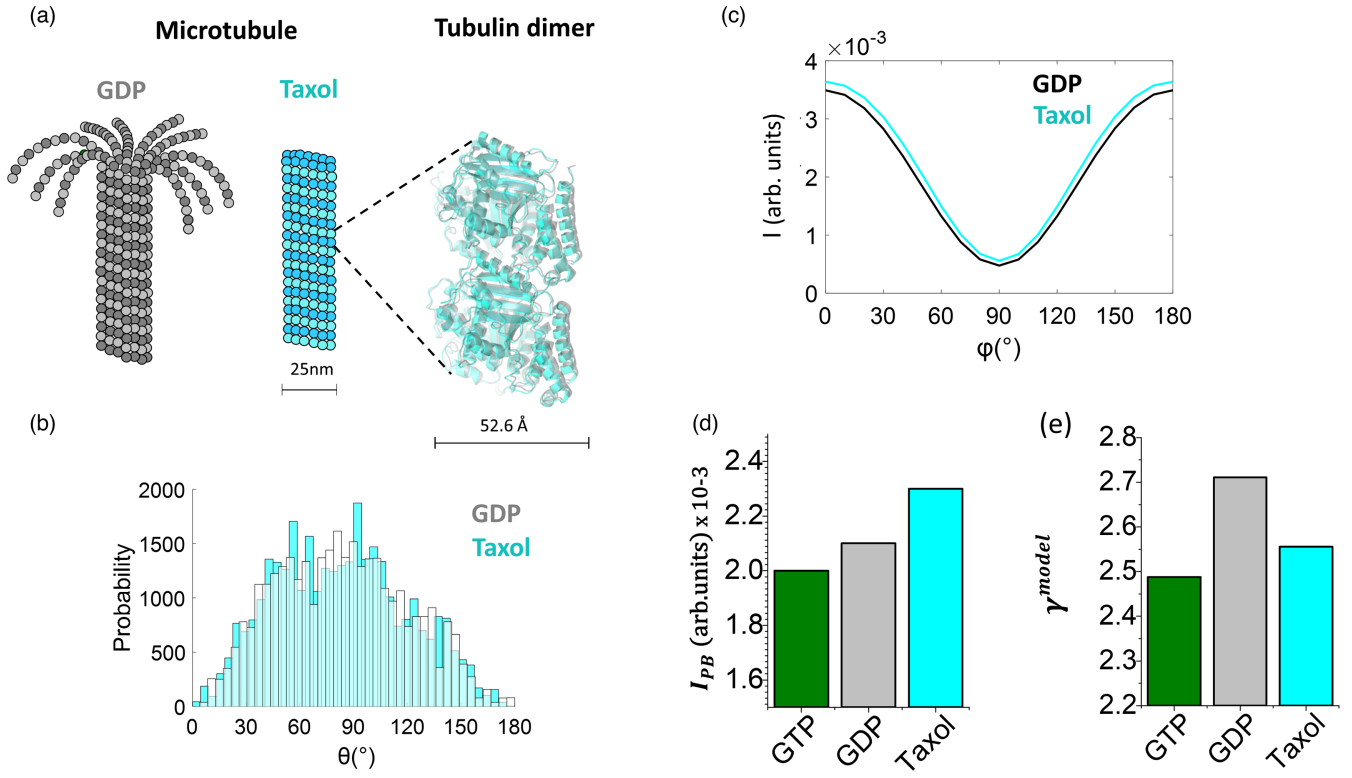

FIG. 5. Modeling pSHG from different microtubule molecular conformations. (a) Microtubule and tubulin dimer in GDP-bound conformation (gray) that is highly unstable and stabilized by taxol drug (cyan). High resolution structures are extracted from Ref. [58]. Tubulin dimer molecular structure is represented with CCP4 molecular graphics. (b) Distribution of $\theta_{zz'}$ angles between the peptide bond axis z' and the laboratory z axis in GDP-tubulin (gray) and taxol-bound tubulin (cyan) microtubule conformation. (c) Simulated SHG intensity per number of peptide bond as a function of the polarization incident angle φ in GDP-tubulin (black) and taxol-bound tubulin (cyan) microtubule conformations. (d),(e) Modeled average SHG intensity per peptide bond averaged over all the incident polarization angles φ (d) and anisotropy factor γ (e) in GTP-tubulin (green), GDP-tubulin (gray), and taxol-bound tubulin (cyan) microtubule conformations.

GTP-tubulin, and taxol-bound tubulin) whose structures have been determined by CryoEM with high resolution by Alushin *et al.* [58]. Changes in microtubule biochemical state lead to a structural rearrangement of the secondary structures of the tubulin dimer [Ref. [58] and Fig. 5(a)] that is reflected by a subtle change in distribution of the polar angles $\theta_{zz'}$ of the PBs with respect to the microtubule axis [Fig. 5(b) and Table II]. The simulated pSHG profiles per PB in microtubule have slightly different amplitudes for the different microtubule molecular configurations considered [Fig. 5(c)], and therefore the computed average SHG intensity per PB (I_{PB}) has different magnitudes [Table II and Fig. 5(d)]. Our simulations indicate that microtubules stabilized by taxol have the highest SHG intensity per PB in agreement with Van Steenbergen *et al.* [17] who observed experimentally an overall increase of SHG intensity in microtubules stabilized by taxol. Our model predicts a similar average SHG intensity per PB for

TABLE II. Modeling different tubulin molecular conformations associated with microtubule (de)polymerization.

Protein	I_{PB} [a]	β_{PB}^{eff}	$\gamma = \sqrt{\frac{I(\varphi_0)}{I(\varphi_0+90°)}}$	$\frac{\beta_{zzz}}{\beta_{zxx}}$	$\bar{\theta}_{zz'}$ [b]	$SD(\theta_{zz'})$	DCS
Microtubule (GTP-tubulin)	0.0020	0.0448	2.488	2.494	83.35°	36.73°	0.010
Microtubule (GDP-tubulin)	0.0021	0.0461	2.711	2.713	83.32°	36.32°	0.017
Microtubule (taxol-bound tubulin)	0.0023	0.0478	2.556	2.557	82.87°	36.52°	0.012

[a]The simulated average SHG intensity per PB (I_{PB}), the effective protein hyperpolarizability per PB (β_{PB}^{eff}), the $\beta_{zzz} = \beta_{zxx}$ ratio calculated with SHG intensities, the anisotropy factor γ_β calculated with the hyperpolarizability tensor components, and deviation from the cylindrical symmetry are calculated as described in Appendix A 10.

[b]The average $\bar{\theta}_{zz'}$ and the standard deviation $SD(\theta_{zz'})$ of the angular distribution of the PBs are extracted from the molecules structure of the proteins as described in Appendix A 6.

GTP-tubulin and GDP-tubulin configuration, while Van Steenbergen *et al.* [17] reported higher hyperpolarizabilities for GTP-tubulin dimers using HRS. The reason for this disparity could potentially be attributed to the fact that our model neglects the aromatic amino acid contribution or to a possible aggregation of dimers in HRS solution. More importantly, we point out that using uniquely SHG intensity to experimentally probe microtubule conformation [17] is challenging because in GTP-tubulin microtubules there is also a decrease in dimer density (tubulin dimer axial repeat change of 2.4% from GTP-tubulin to GDP-tubulin conformation [58]) as well as a macromolecular rearrangement of microtubule organization and alignment that affect the SHG efficiency. On the other hand, the evaluation of the anisotropy factor γ represents a more robust measurement since it is ratiometric. We evaluated the anisotropy factor γ for the different microtubule conformations [Fig. 5(e)]. Our simulations show that taxol-bound tubulin configuration has a higher value of γ compared to GDP-like structure as previously reported experimentally [38,39]. We also found similar values of the anisotropy factor γ for GTP-tubulin and taxol-bound tubulin states confirming that no major conformational differences are observed at the molecular level between these two states, while their molecular structure differs from the structure of GDP-tubulin [58].

Overall, our simulations demonstrate the exquisite sensitivity of our model to the molecular structure of microtubules associated with different biochemical states and stability by predicting changes both in SHG intensity and in anisotropy factor γ in stabilized microtubules [Figs. 5(d) and 5(e)]. This result shows the promise of this bottom-up approach to predict and elucidate molecular level alterations due to either mutations or post-translational modifications that might occur in different types of diseases; recent work indeed demonstrated that a mutation can affect the structure of a protein as well as its hyperpolarizability [79]. Our modeling could be, for example, helpful to quantitatively interpret SHG measurement [13,17] in the context of interaction with microtubules associated proteins such as tau [80]. We anticipate that this modeling will help us understand how tau protein stabilizes bundles of axonal microtubules at the molecular and macromolecular level and how it fails to do it in the context of neurodegenerative diseases [81–83], as well as the dynamic interplay between microtubule molecular conformation and molecular motors such as kinesis [39] that are essential for axonal transport. Our modeling would also be relevant to cardiopathies by interpreting the deviation from the healthy pSHG anisotropy factor due to myosin mutations [36] in terms of myosin molecular and structural conformation [11].

III. CONCLUSIONS

In this work, we established and experimentally validated a comprehensive bottom-up numerical model for predicting SHG of protein assemblies from their molecular structure and for identifying different protein types, conformations, or assemblies in pSHG images. Our model links the micrometer-scale measurements provided by SHG microscopy to the proteins' atomic-scale structure as determined by CryoEM, x-ray crystallography, or deep learning based approaches [84–86]. The main novelty of our model is that it is based on a simple hypothesis (SHG dipole along the peptide bond, unique hyperpolarizability tensor component) without any quantum mechanical calculations of building blocks, so that it can be used for any protein with a complex 3D structure, not just simple and small proteins with helical structure like collagen. Moreover, besides the hyperpolarizability, our model provides the calculation of a series of parameters of interest (the anisotropy factor as well as the SHG intensity per peptide bond and the deviation from cylindrical symmetry) for the identification and the comparison of different proteins. Using the spatial distribution of PBs within the protein assemblies extracted from their atomic coordinates in the PDB, we calculated the second-order hyperpolarizability tensor β_{ijk}. We then predicted the resulting pSHG profiles as a function of the polarization incident angle φ and analyzed the deviation from cylindrical symmetry (Fig. 2 herein and Fig. S7 in Supplemental Material [47]). Our model predicts SHG efficiency (I_{PB}) and anisotropy factor γ for collagen, myosin, microtubules, and actin that are in good agreement with experimental measurements in live zebrafish larvae (Fig. 3) and consistent with previously published observations.

Our work clearly demonstrates with both experiments and modeling that pSHG and the anisotropy factor γ can be used to discriminate the three main sources of endogenous SHG in biological tissues (collagen, myosin, and microtubule), which establishes the specificity of this label-free imaging method [Figs. 1(f), 1(h), 3(a), and 3(h)]. We further combine pSHG analysis with automatic detection of fiber orientation and thus provide the first demonstration of automated identification of proteins from their pSHG signal independently of fiber orientation. We also demonstrate that the observed γ value ranges for these proteins ([01] for myosin, [12] for collagen, and [23] for microtubule) have a fundamental origin in the molecular structures of these proteins.

This comprehensive bottom-up computational approach unveiled the dependence of these parameters on the 3D distribution of peptide bonds within the proteins [Figs. 3(e)–3(g)]. We showed that such a model is necessary to account for SHG by protein and assemblies with broad distribution of PB orientations such as microtubules and protein complexes. In contrast, commonly used simplified model using a single polar angle fails at predicting SHG from such structures (Table VII).

With this computational framework, we also estimated absolute values of the effective susceptibility of small

polypeptides and obtained results consistent with HRS measurements in collagen [42] and tubulin [17] (Table VIII). We predicted the dependence of pSHG in microtubule assemblies on their 3D macromolecular arrangement, revealing a specific dependence on the out-of-plane angle, the angular spread, and the polarity of microtubule assemblies (Fig. 4). Finally, using published structural information, we demonstrated the sensitivity of our modeling to the changes in the molecular conformations of microtubules (GTP-tubulin, GDP-tubulin, and taxol-bound tubulin) associated with their (de)polymerization state (Fig. 5), opening the way to quantitative interpretation of SHG signal in terms of conformational changes of microtubules and of their interaction with microtubule associated proteins [38,39,81].

The fact that values of I_{PB}, β_{PB}^{eff}, and γ predicted with our model are generally consistent with experiments validates this model and its approximations. We showed that the assumption of plane wave has a little influence on the prediction of the anisotropic factor. In the context of more scattering or in anisotropic tissues in which diattenuation, birefringence, and imaging depth are not negligible, a model accounting for these parameters would be necessary to predict correctly the anisotropic factor γ [63,65,66]. Also, we considered only the PB contributions to SHG and neglected the contribution of aromatic amino acids. This approximation looks reasonable not only in proteins without aromatic amino acids (collagen and myosin tail) but also in tubulin, where aromatic amino acids are more abundant. Despite their significantly bigger hyperpolarizability with respect to PBs (≈2–7 fold) [43,61,62], aromatic amino acids might not contribute significantly to the SHG contrast because their signal cancels out due to their random orientation within the protein. Integrating the contributions of aromatic amino acids would possibly allow a more precise prediction of SHG from structures with large number of such residues, such as tubulin assemblies, where their organization may also depend on the protein molecular conformation. However, we note that, despite neglecting the aromatic amino acids, we already have a good prediction of SHG generation (I_{PB}) and anisotropy factor γ in different molecular conformations (GDP-tubulin, GTP-tubulin, and taxol-bound tubulin) of microtubules.

In conclusion, we demonstrated that a bottom-up multiscale model precisely accounts for the structural information held in pSHG measurements. This methodological advance holds promise for developing pSHG microscopy into an ultrastructural probe, able to detect allosteric biochemical changes and protein structural rearrangements during physiopathological processes. We believe that our model creates a foundation to elucidate protein structural alterations in different contexts such as neurodenenerative diseases and cardiomyopaties. For example, accurate pSHG modeling opens opportunities to shed light on supramolecular arrangements of β-sheet assemblies in amyloid proteins misfolding and fibrils aggregations [87], helping us to understand aberrant organizations observed in neurodegenerative diseases [88,89]. Our method could also be used for characterizing organized biomaterials and scaffolds in the context of tissue engineering [90,91] as well as to guide the design of proteins and materials that have strong SHG efficiency.

All data and scripts and codes written in MATLAB or data analysis and modeling will be uploaded in the Zenodo repository [92].

ACKNOWLEDGMENTS

This work was supported by the Agence Nationale de la Recherche (ANR) under Contracts No. ANR-10-INBS-04 France BioImaging, No. ANR-11-EQPX-0029 Morphoscope2, and No. ANR-15-CE11-0012-01 NLOMMIT. We thank Emilie Menant for zebrafish husbandry and Guy Malkinson for early work on tubulin SHG signal detection in the zebrafish brain.

C. S., E. B., and W. S. designed the experiments. E. B., C. S., and P. M. implemented the microscopy setup. B. A. performed experiments and analyzed the data. C. S. designed the modeling and performed the numerical calculations. C. S. and M.-C. S.-K. designed and performed the analytical calculations. X. Z. and A. C. developed the workflow for automated fiber detection.

The authors declare no conflicts of interest.

APPENDIX: MATERIAL AND METHODS

1. Polarization resolved SHG microscopy in zebrafish embryos

We performed pSHG imaging on a custom-built laser scanning two-photon upright microscope that is equipped with a femtosecond laser source (80 MHz, 1150 nm, 100 fs, Insight X3, Spectra-Physics, Santa Clara, CA, U.S.), galvanometric scanners (VM500S, GSI Lumonics, Bedford, MA, U.S.), and a water immersion objective (25×, 1.05 NA, XLPLN25XWMPm Olympus, Japan). The SHG signal was forward collected, using a high NA condenser (Olympus, Japan), GaAsP detector (Hamamatsu H7422-40 GaAsP detectors, Japan), and bandpass filter (Semrock FF01575/19 nm). Polarization control was performed with a rotating half-wave plate (Fichou, France) before the objective, as described in a simplified schematic of microscope in Fig. 1(a). The polarization control and the image acquisition was performed using a custom written software written in LabView (National Instruments, U.S.) and an I/O board (PCI-6115, National Instruments, Austin, TX, U.S.).

We performed SHG imaging on a zebrafish embryo from a wild type fish line at 5 days post fertilization (5 dpf). After anesthetizing the embryos in 0.16 mg/mL in Tricaine (MS-222 Sigma, cat E10521, St. Louis, MO, U.S.) solution for

TABLE III. Imaging parameters in Fig. 1.

Protein or structure	Power (mW)	Pixel dwell time (μs)	Depth (μm)	N photons	$\bar{\gamma} \pm \sigma$
Collagen	10	10	20	852	1.63 ± 0.16
Myosin	30	5	20	1014	0.46 ± 0.04
Tubulin	100	20	100	217	2.23 ± 0.43
Collagen in collagen + myosin	20	10	20	794	1.62 ± 0.11
Myosin in collagen + myosin	20	10	20	459	0.46 ± 0.13

10 minutes, we embedded them in 1% low melting point agarose (Invitrogen, cat 15517014, Carlsbad, CA, U.S.) for imaging adding Tricaine. The acquisition of pSHG images was performed every 10° from 0° to 180°. The acquisition time of a pSHG stack was on the order of 20–90 sec for a 100×100–500×500 pixels image with pixel dwell time of 5–20 μs/pixel with a 10–100 mW excitation power and a signal level of typically 200–1000 photons/pixel for the sum of polarizations (See Table III). The mean powers used for imaging collagen, myosin, and microtubules are 10, 30, and 100 mW, respectively (see Table III). We performed imaging of collagen in the pectoral fin at 20 μm depth, myosin in the muscles of the tail at 20 μm depth, and microtubules in the spinal cord were imaged at a depth of 100 μm in zebrafish embryos from the dorsal side [see Fig. 1(b)]. We determined experimentally a power limit of 100 mW to perform pSHG measurements in live 5 days post fertilization (dpf) zebrafish embryos without inducing visible damage. After imaging we kept the fish alive for another 24 hours and we verified their survival and correct development. We performed imaging of the pectoral fin at 20 μm depth where collagen fibers and muscle fibers are present in the same region in zebrafish embryos imaged from the dorsal side.

2. Image analysis

Image analysis was done using Fiji [93] (NIH, Bethesda, MD, U.S.), a custom written program in MATLAB and PYTHON code. We first registered the pSHG stack with the plugin StackReg in Fiji to correct possible translation moving artifacts. We performed fitting of the pSHG curved extracted data [Fig. 1(d) herein and Table IV] from different ROIs with Eq. (A21) in Appendix A 10.

Pixel-by-pixel fiber angle mapping was performed with structure-tensor analysis [94,95], using a structure-tensor based method [48]. Briefly, we first apply a median filter to denoise the raw image, we then compute the structure tensor $S = \overline{\nabla I (\nabla I)^T}$, that is the outer product of the gradient vector with itself, then locally averaged within a neighborhood. $\nabla I = [I_x I_y]^T$ is the gradient vector. In 2D images, the structure tensor for each pixel is a 2×2 matrix:

$$S = \begin{bmatrix} \overline{I_x^2} & \overline{I_x I_y} \\ \overline{I_x I_y} & \overline{I_y^2} \end{bmatrix}.$$

The structure tensor is computed using two Gaussian filters. We convolve I with derivatives of Gaussian along x and y with standard deviation σ to obtain I_x and I_y. We convolve each value with a Gaussian kernel with standard deviation ρ, which is the size of the neighborhood for averaging. We used $\sigma = 1$ and $\rho = 20$. ρ can be adjusted based on the size of the structures of the image. Finally, we perform eigendecomposition of the structure tensor S that yields two positive eigenvalues $\lambda_1 \leq \lambda_2$ corresponding to two orthogonal eigenvectors e_1 and e_2. The smallest eigenvalue λ_1 means the orientation represented by e_1 has the smallest variation in intensity and is the predominant orientation of the pixel. Since e_1 is a unit vector (v_x, v_y) we compute the orientation of every pixel with $\theta = \tan^{-1}(v_y/v_x)$ to create the fiber angle maps (Figs. S1, S2g, and S3f in Ref. [47]).

Pixel-by-pixel pSHG analysis was performed with MATLAB (Mathworks, Natick, MA, U.S.) using a program based on fast Fourier transform (FFT) [50,96]. For every pixel we determined the first three complex Fourier coefficients (F0, F1, and F2). We first used the phase of the F1 coefficient (Figs. S1b, S2f, and S3e [47]) to calculate an orientation angle that indicates the absolute angle of the maximum (highest minimum) SHG intensity for one-peaked (two-peaked) pSHG profiles. We then determined the relative angle of the maximum (highest minimum) SHG intensity with respect to the fiber axis for one-peaked (two-peaked) pSHG profiles [Fig. 1(e) herein and Figs. S1, S2h, and S3g in Ref. [47]) by subtracting the phase of F1 and the angle of the fiber, that was previously determined in every pixel (Fig. S1 [47]). We then calculated the anisotropy factor $\gamma = \sqrt{I_\parallel / I_\perp}$, where $I_\parallel$ is the SHG intensity parallel to the fiber axis and $I_\perp$ is the SHG intensity perpendicular to the fiber axis (Fig. S1). For proteins with the maximum (highest minimum) SHG intensity at 0° with respect to

TABLE IV. Fitted parameters in Fig. 1(d).

Protein	γ	R^2
Collagen	1.59 ± 0.07	0.98
Myosin	0.56 ± 0.04	0.94
Microtubules	2.44 ± 0.07	0.98
Collagen in collagen + myosin	1.45 ± 0.02	0.97
Myosin in collagen + myosin	0.57 ± 0.05	0.94

the fiber axis, such as collagen and microtubule, $I_{\parallel} = |F_0| + |F_1| - |F_2|$ and $I_{\perp} = |F_0| - |F_1| - |F_2|$. For proteins with the maximum (highest minimum) SHG intensity at 90° with respect to the fiber axis, such as myosin, $I_{\parallel} = |F0| - |F1| - |F_2|$ and $I_{\perp} = |F_0| + |F_1| - |F_2|$. We then applied a 2×2 median filter to the γ and angles matrices to reduce the noise without reducing the spatial resolution (Fig. S1c [47]). The reliability of this calculation is determined by the R^2 parameter that compares the experimental data and the curve obtained from the extracted Fourier coefficients. We selected pixels of the images with a R^2 greater than 0.4 (Figs. S1d and S1e [47]). For pSHG images in which different types of protein are present, we take into account the direction of the fibers and the relative angle of the maximum (highest minimum) SHG intensity to calculate the anisotropy factor. Calculations on the SHG efficiency in every protein was performed by normalizing the SHG images by the square of the power used.

3. Experimental imaging parameters and pSHG measurement precision

As we adapted the imaging conditions to different endogenous proteins, we report in Table III the experimental parameters, the total number of photons over the polarizations for the regions of interests in Fig. 1(c), as well as the average and the standard deviation of the anisotropy factor γ calculated over the pixels in Figs. 1(f) and 1(h).

To estimate the precision of the pSHG measurement, we evaluated the theoretical expected standard deviation of γ as a function of the total number of photons N_{tot} as derived in Refs. [49,50] [Fig. 1(i)].

4. Fit of experimental pSHG profiles

We fitted the experimental pSHG profiles obtained from a region of interest of Fig. 1(d) with the cylindrical symmetry [Eq. (A21) in Appendix A 10] and we obtained the parameters in Table IV.

We note that the error of the γ calculated in a ROI (Table IV) is smaller with respect to the average error calculated on the single pixels (Table III) because the SNR in the ROI is significantly better than in the single pixels.

5. Theoretical background of SHG response

A material response to an applied electric field E is described by the induced polarization $\vec{P}$:

$$P = \epsilon_0(\chi^{(1)}E + \chi^{(2)}E^2 + \chi^{(3)}E^3 + \cdots), \tag{A1}$$

where $\chi^{(n)}$ is the nth-order nonlinear susceptibility. The $\chi^{(2)}$ tensor describes the second-order susceptibility tensor and is a third rank tensor with 18 elements in the specific case of SHG [97]. The $\chi^{(2)}$ tensor probed experimentally with a focused laser beam is determined by the ensemble of the nonlinear optical responses and the spatial distribution of the molecules within the excitation volume. The molecular nonlinear properties are described by the first hyperpolarizability tensor β, where $p = \beta E^2$ is the second-order induced molecular dipole moment. The molecular and the bulk properties are related by the following equation:

$$\chi^{(2)} = N\langle\beta\rangle/\epsilon_0, \tag{A2}$$

where N is the density of the molecules and the bracket denotes the orientational average. As SHG is characterized by energy and phase conservation, all the waves radiated by the molecules in the micrometer-scale focal volume coherently sum up. In order to have a nonzero $\chi^{(2)}$ at this scale, molecules with a nonzero dipole moment must exhibit a preferential polarity, leading to constructive interference of the second-harmonic waves. Therefore, the bulk properties of a material are determined by both the values of the molecular hyperpolarizabilities and the organization and the degree of alignment of the emitters inside the focal volume. The second-order induced polarization depends on the second-order susceptibility tensor $\chi^{(2)}_{ijk}$ and the excitation electric field as follows:

$$\begin{pmatrix} P_x^{(2)} \\ P_y^{(2)} \\ P_z^{(2)} \end{pmatrix} = \begin{pmatrix} \chi^{(2)}_{xxx} & \chi^{(2)}_{xyy} & \chi^{(2)}_{xzz} & \chi^{(2)}_{xyz} & \chi^{(2)}_{xxz} & \chi^{(2)}_{xxy} \\ \chi^{(2)}_{yxx} & \chi^{(2)}_{yyy} & \chi^{(2)}_{yzz} & \chi^{(2)}_{yyz} & \chi^{(v)}_{yxz} & \chi^{(2)}_{yxy} \\ \chi^{(2)}_{zxx} & \chi^{(2)}_{zyy} & \chi^{(2)}_{zzz} & \chi^{(2)}_{zyz} & \chi^{(2)}_{zxz} & \chi^{(2)}_{zxy} \end{pmatrix} \begin{pmatrix} E_x^2 \\ E_y^2 \\ E_z^2 \\ 2E_yE_z \\ 2E_xE_z \\ 2E_xE_y \end{pmatrix}. \tag{A3}$$

Far from resonance the susceptibility tensor $\chi^{(2)}_{ijk}$ is independent of the frequency of the electric field; therefore, all indices of the tensor may be freely permuted, a condition that is known as Kleinman symmetry [98]. It reduces to 10 the number of independent elements of the susceptibility tensor.

Since many sources of SHG are protein assemblies with a cylindrical symmetry, we consider this particular case. For a material with cylindrical symmetry the second-order susceptibility tensor will have several null elements as well as several equal elements [97]. A cylindrical symmetry around the z axis (corresponding to the mirror planes xz and yz) leads to an invariance for the transformation $x \to y$ and $y \to -x$, hence obtaining $\chi^{(2)}_{yyz} = \chi^{(2)}_{(-x)(-x)z} = \chi^{(2)}_{xxz}$, and for Kleinman symmetry:

$$\chi^{(2)}_{zxx} = \chi^{(2)}_{xxz} = \chi^{(2)}_{zyy} = \chi^{(2)}_{yyz}. \tag{A4}$$

Therefore, for a material with a cylindrical symmetry around the z axis, $\chi^{(2)}_{zzz}$ and $\chi^{(2)}_{zxx}$ are the only two

independent components of the susceptibility tensor, while the others vanish due to symmetry of the material:

$$\chi^{(2)}_{\mathrm{cyl}} = \begin{pmatrix} 0 & 0 & 0 & 0 & \chi^{(2)}_{xxz} & 0 \\ 0 & 0 & 0 & \chi^{(2)}_{yyz} & 0 & 0 \\ \chi^{(2)}_{zxx} & \chi^{(2)}_{zyy} & \chi^{(2)}_{zzz} & 0 & 0 & 0 \end{pmatrix}. \quad \text{(A5)}$$

6. Extraction of peptide bonds distribution from protein molecular structure in the Protein Data Bank

In our model we assume that the elementary SHG emitters are located along the PB C-N between every amino acid of the protein, as the PB presents a partial charge transfer due to the electronic $\pi \rightarrow \pi^*$ transition [Fig. 2(a)]. For every amino acid (AA) of the protein, we first extract the positions of all the carbon $\vec{\mathrm{C}} = (X_{\mathrm{C}}, Y_{\mathrm{C}}, Z_{\mathrm{C}})$ and nitrogen $\vec{\mathrm{N}} = (X_{\mathrm{N}}, Y_{\mathrm{N}}, Z_{\mathrm{N}})$ atoms belonging to the amide groups along the protein backbone. We then define the SHG harmonophore associated with the PB n as the vector $\vec{\mathrm{N}}(n+1) - \vec{\mathrm{C}}(n)$ from the carbon atom of the amino acid n to the nitrogen atom of the amino acid $n+1$ and we determine the axes $z'(n)$ of every peptide bond reference system with respect to the laboratory system xyz [Fig. 2(b)]. The orientation of the peptide bond $z'(n)$ axis with respect to the laboratory reference system xyz is defined by the set of angles $\theta_{xz'(n)}\theta_{yz'(n)}\theta_{zz'(n)}$.

For every protein of interest we reconstructed the three-dimensional distribution of the PBs [Fig. 2(c) herein and Figs. S5 and S6 and Movies M7–M11 in Supplemental Material [47]], the distribution of the polar angle $\theta_{zz'(n)}$ between the PB axis $z'(n)$ and the laboratory axis z [Fig. 2(d) herein and Fig. S5c [47]], as well as the distribution of the PB length (not shown). We calculated the mean values $\bar{\theta}_{zz'(n)}$ and the standard deviation $\mathrm{SD}(\theta_{zz'(n)})$ of the $\theta_{zz'(n)}$ angle distribution [Fig. 3(e) and Table I].

We reconstructed the protein 3D distribution of PBs for the following proteins as summarized in Table V:

(i) the triple helix $[(\text{Pro-Pro-Gly})_{10}]_3$ (PPG10) from the 1K6F.pdb file [56] taking into account A, B, C, D, E, and F chains of the protein for a total of 166 PBs (Movie M7 [47]).

TABLE V. Extraction of peptide bond distribution in different proteins.

Protein	PDB ID	N_{PB}	Chains	Reference
Collagen	1K6F	166	A–F	[56]
Myosin tail	2FXO	248	A–B	[57]
Tubulin dimer GTP-tubulin)	3J6E	851	A–B	[58]
Microtubule (GTP-tubulin)	3J6E	33 131	A–R	[58]
Microtubule (GDP-tubulin)	3J6F	33 104	A–R	[58]
Microtubule (taxol-bound tubulin)	3J6G	33 133	A–R	[58]
Actin	6BNO	2927	A–H	[59]

(ii) the α-helical coiled-coil tail of the myosin protein from the 2FXO.pdb file [57] taking into account A and B chains of the protein for a total of 248 PBs (Movie M8 [47]).

(iii) the tubulin dimer (α and β monomers) from the microtubule segment in GTP-tubulin conformation from the 3J6E.pdb file [58] taking into account A and B chains for a total of 851 PBs (Movie M9 [47]).

(iv) the microtubule from the microtubule segment in GTP-tubulin (3J6E.pdb file), GDP-tubulin (3J6F.pdb file), and taxol-bound tubulin (3J6G.pdb file) conformations [58] taking into account A, B, C, D, E, F, G, H, I, J, K, L, M, N, O, P, Q, and R chains. We reconstructed manually the entire structure of the microtubule with a tubular structure of 24 nm diameter with 13 protofilaments for a total of 39 tubulin dimers and ∼33 000 PBs (Movie M10 [47]).

(v) the actin filament from the 6BNO.pdb file [59] taking into account A, B, C, D, E, F, G, and H chains for a total of 2927 PBs (Movie M11 [47]).

In the PDB files of collagen, microtubule, and actin the protein axis z_p is aligned with the z axis of the laboratory system. On the other hand, we rotate the myosin tail to align its fiber axis z_p with the z axis.

7. 3D rotation of protein

We implemented a module to perform a specific 3D rotation of the protein atoms coordinates in order to align the protein axis of the PDB file along the z axis or to rotate the protein of interest in the 3D space to simulate a specific molecular assembly. We apply the following transformation:

$$\begin{pmatrix} x_F \\ y_F \\ z_F \end{pmatrix} = \begin{pmatrix} \cos p \cos s - \sin p \sin t & \sin p \cos t & \cos p \sin s + \sin p \sin t \\ -\sin p \cos s - \cos p \sin t \sin s & \cos p \cos t & -\sin p \sin s + \cos p \sin t \cos s \\ -\cos t \sin s & -\sin t & \cos t \cos s \end{pmatrix} \begin{pmatrix} x_I \\ y_I \\ z_I \end{pmatrix}, \quad \text{(A6)}$$

where t, p, and s are the angles of rotation with respect to the x, z, and y axis, respectively. To rotate the microtubule out of the plane of imaging yz, we introduced a rotation around the y axis (s angle) from 0° to 90° with a step of 10°. To simulate an angular dispersion we consider a linear distribution of microtubules with out-of-plane angles. To simulate microtubule with different polarity we rotate the microtubule around the y axis (s angle) of 180° to obtain a microtubule of opposite polarity.

8. Calculation of second-order protein hyperpolarizability

From the distribution of peptide bonds of a given protein, we estimated every element β_{ijk} of the second-order hyperpolarizability of the protein summing each individual hyperpolarizability term $\beta_{i'j'k'}$ of the PBs and taking into account their relative orientation with respect to the protein system, using the following formula:

$$\beta_{ijk} = \sum_{n=1}^{N_{\mathrm{PB}}} \sum_{i'j'k'} \cos\theta_{ii'(n)} \cos\theta_{jj'(n)} \cos\theta_{kk'(n)} \beta_{i'(n)j'(n)k'(n)}, \tag{A7}$$

where θ are the angles of the PBs reference system with respect to the xyz laboratory system [Fig. 2(b)] and N_{PB} is the total number of PBs within a protein. Under the assumptions that the PB has a preferred hyperpolarizability axis along the C—N bond axis (z') [Figs. 2(a) and 2(b)], we consider the only nonzero component of the hyperpolarizability tensor $\beta_{z'z'z'}$. We further assume that the $\beta_{z'z'z'}$ of the peptide bond is insensitive to the residues [R in Fig. 2(a)] of the ammino acids. We therefore can express the protein hyperpolarizability tensor as follows:

$$\beta_{ijk} = \sum_{n=1}^{N_{\mathrm{PB}}} \cos\theta_{iz'(n)} \cos\theta_{jz'(n)} \cos\theta_{kz'(n)} \beta_{z'(n)z'(n)z'(n)}, \tag{A8}$$

where for every PB, $\cos\theta_{xz'(n)} = (X_{N(n+1)} - X_{C(n)})/L$, $\cos\theta_{yz'(n)} = (Y_{N(n+1)} - Y_{C(n)})/L$ and $\cos\theta_{zz'(n)} = (Z_{N(n+1)} - Z_{C(n)})/L$, and L is the length of the peptide bond $L_{(n)} = |N(n+1) - C(n)|$. Finally, we computed every component of the second-order hyperpolarizability tensor β_{ijk} normalized by the number N_{PB} of PBs $\beta_{\mathrm{PB}} = \beta/N_{\mathrm{PB}}$ for every protein [Eqs. (A10)–(A16)].

9. Computation of protein hyperpolarizability tensor per peptide bond

We computed the protein second-order nonlinear hyperpolarizability tensor,

$$\beta_{\mathrm{PB}} = \begin{pmatrix} \beta_{xxx} & \beta_{xyy} & \beta_{xzz} & \beta_{xyz} & \boldsymbol{\beta_{xxz}} & \beta_{xxy} \\ \beta_{yxx} & \beta_{yyy} & \beta_{yzz} & \boldsymbol{\beta_{yyz}} & \beta_{yxz} & \beta_{yxy} \\ \boldsymbol{\beta_{zxx}} & \boldsymbol{\beta_{zyy}} & \boldsymbol{\beta_{zzz}} & \beta_{zyz} & \beta_{zxz} & \beta_{zxy} \end{pmatrix}, \tag{A9}$$

normalized by the number N_{PB} of PBs by using Eq. (A8) from the PDB atomic reconstruction of collagen [56], myosin tail [57], microtubules [58], and actin [59]. The tensor components that are expected to be different from zero in the case of hypothesis of cylindrical symmetry are represented in bold. All the components of β_{PB} are normalized to the hyperpolarizability $\beta_{z'z'z'}$ of one PB and multiplied by a factor of 100.

As an example of processing speed, the calculations of $\beta_{\mathrm{PB}}^{\mathrm{MT}}$ in Eq. (A13) for a microtubule with 33 131 PBs (Table V) took 0.02 sec on a laptop PC equipped with Intel Core i7-10610U processor and 16 GB of RAM.

$$\beta_{\mathrm{PB}}^{\mathrm{collagen}} = \begin{pmatrix} 0.37 & -0.64 & -0.57 & 0.39 & \mathbf{-17.68} & 0.46 \\ 0.46 & -0.36 & 0.04 & \mathbf{-17.87} & 0.39 & -0.64 \\ \mathbf{-17.68} & \mathbf{-17.87} & \mathbf{-24.96} & 0.04 & -0.57 & 0.39 \end{pmatrix}, \tag{A10}$$

$$\beta_{\mathrm{PB}}^{\mathrm{myosin}} = \begin{pmatrix} 1.34 & 0.22 & 0.39 & 0.07 & \mathbf{-11.50} & 0.08 \\ 0.08 & 0.43 & -0.15 & \mathbf{-12.89} & 0.07 & 0.2 \\ \mathbf{-11.50} & \mathbf{-12.89} & \mathbf{-5.63} & 0.11 & 0.39 & 0.07 \end{pmatrix}, \tag{A11}$$

$$\beta_{\mathrm{PB}}^{\mathrm{dimer-GTP}} = \begin{pmatrix} 2.29 & 2.69 & -0.61 & -0.98 & \mathbf{-1.53} & 0.66 \\ 0.66 & -0.45 & -1.91 & \mathbf{-3.03} & -0.98 & 2.69 \\ \mathbf{-1.53} & \mathbf{-3.03} & \mathbf{-5.67} & -1.91 & -0.61 & -0.98 \end{pmatrix}, \tag{A12}$$

$$\beta_{\mathrm{PB}}^{\mathrm{MT-GTP}} = \begin{pmatrix} -0.02 & 0.03 & 0 & -0.01 & \mathbf{-2.25} & 0 \\ 0 & -0.02 & 0 & \mathbf{-2.26} & -0.01 & 0.03 \\ \mathbf{-2.25} & \mathbf{-2.26} & \mathbf{-5.62} & 0 & 0 & -0.01 \end{pmatrix}, \tag{A13}$$

$$\beta_{\mathrm{PB}}^{\mathrm{MT-GDP}} = \begin{pmatrix} -0.02 & 0.02 & 0 & -0.01 & \mathbf{-2.18} & 0 \\ 0 & -0.01 & 0.01 & \mathbf{-2.18} & -0.01 & 0.02 \\ \mathbf{-2.18} & \mathbf{-2.18} & \mathbf{-5.91} & 0.01 & 0 & -0.01 \end{pmatrix}, \tag{A14}$$

$$\beta_{\mathrm{PB}}^{\mathrm{MT-taxol}} = \begin{pmatrix} -0.01 & 0.02 & 0 & -0.01 & \mathbf{-2.35} & 0 \\ 0 & -0.01 & 0.01 & \mathbf{-2.36} & -0.01 & 0.02 \\ \mathbf{-2.36} & \mathbf{-2.36} & \mathbf{-6.03} & 0.01 & 0 & -0.01 \end{pmatrix}, \tag{A15}$$

$$\beta_{\mathrm{PB}}^{\mathrm{actin}} = \begin{pmatrix} 0.27 & 0.24 & 0.18 & 0.22 & \mathbf{0.16} & 0.02 \\ 0.02 & -0.15 & -0.12 & \mathbf{0.20} & 0.22 & 0.24 \\ \mathbf{0.16} & \mathbf{0.20} & \mathbf{-0.63} & -0.12 & 0.18 & 0.22 \end{pmatrix}. \tag{A16}$$

10. Modeling pSHG from a protein

Once the second-order hyperpolarizability of every protein is calculated from the 3D distribution of PBs, we proceed to model the pSHG response. We assumed a plane wave with the incident electric field $\vec{E}(\omega) = (E_x, E_y, E_z)$ that propagates along the x direction and it is linearly polarized in the yz plane with a direction of angle φ with respect to the axis of the protein along z [Fig. 2(b)], while we estimate the error introduced by the approximation of plane wave at the focal point in Supplemental Material B [47]. Therefore, we can express the components of the electric field as follows:

$$E_x = 0, \qquad E_y = E\sin\varphi, \qquad E_z = E\cos\varphi. \tag{A17}$$

We calculated the second-order induced dipole $\vec{p} = \beta_{\mathrm{PB}}\vec{E}\,\vec{E}$ as a function of the angle φ both for the general case,

$$\begin{aligned} p_x(\varphi) &= \beta_{xyy}E^2\sin^2\varphi + \beta_{xzz}E^2\cos^2\varphi + \beta_{xyz}E^2\sin 2\varphi, \\ p_y(\varphi) &= \beta_{yyy}E^2\sin^2\varphi + \beta_{yzz}E^2\cos^2\varphi + \beta_{yyz}E^2\sin 2\varphi, \\ p_z(\varphi) &= \beta_{zyy}E^2\sin^2\varphi + \beta_{zzz}E^2\cos^2\varphi + \beta_{zyz}E^2\sin 2\varphi, \end{aligned} \tag{A18}$$

and for the hypothesis of cylindrical symmetry for which only few components of $\beta^{(2)}$ are different from zero,

$$\begin{aligned} p_x^{\mathrm{cyl}}(\varphi) &= 0, \\ p_y^{\mathrm{cyl}}(\varphi) &= \beta_{yyz}E^2\sin 2\varphi, \\ p_z^{\mathrm{cyl}}(\varphi) &= \beta_{zyy}E^2\sin^2\varphi + \beta_{zzz}E^2\cos^2\varphi. \end{aligned} \tag{A19}$$

Note that we consider here the induced dipole and the hyperpolarizability rather then the induced polarization and the susceptibility since we make no hypothesis about the organization at the macromolecular or tissue level. We then model the SHG intensity as a function of the angle φ both for the general case,

$$\mathrm{I}(\varphi) \propto \{[p_x(\varphi)]^2 + [p_y(\varphi)]^2 + [p_z(\varphi)]^2\}, \tag{A20}$$

and for the hypothesis of cylindrical symmetry,

$$\begin{aligned} \mathrm{I}^{\mathrm{cyl}}(\varphi) &\propto \{[p_x^{\mathrm{cyl}}(\varphi)]^2 + [p_y^{\mathrm{cyl}}(\varphi)]^2 + [p_z^{\mathrm{cyl}}(\varphi)]^2\} \\ &\propto (\beta_{zyy})^2[\sin^2 2\varphi + (\sin^2\varphi + \gamma\cos^2\varphi)^2], \end{aligned} \tag{A21}$$

where $\gamma = \sqrt{I^{\mathrm{cyl}}(\varphi_0)/I^{\mathrm{cyl}}(\varphi_0 + 90°)}$, φ_0 is the angle of the fiber axis, $I^{\mathrm{cyl}}(\varphi_0)$ is the SHG intensity parallel to the fiber axis, and $I^{\mathrm{cyl}}(\varphi_0 + 90°)$ is the SHG intensity perpendicular to the fiber axis. In the case of cylindrical symmetry, the anisotropy factor is equivalent to β_{zzz}/β_{zxx}, where β_{zzz} and β_{zxx} are the independent values of the hyperpolarizability tensor.

We note that for both $\mathrm{I}(\varphi)$ and $\mathrm{I}^{\mathrm{cyl}}(\varphi)$ we consider the total amount of SHG radiated, neglecting the effect of experimental detection geometry (numerical aperture of the objective and backward or forward collections).

Five quantitative parameters are considered from the modeling of the pSHG of a protein:

(i) the average SHG intensity per peptide bond over all the incident polarization angles φ, that we associate to the SHG generation efficiency,

$$\mathrm{I}_{\mathrm{PB}} = \langle \mathrm{I}(\varphi) \rangle \tag{A22}$$

(ii) the effective protein hyperpolarizability per peptide bond,

$$\beta_{\mathrm{PB}}^{\mathrm{eff}} = \sqrt{\mathrm{I}_{\mathrm{PB}}} \tag{A23}$$

(iii) the usual anisotropy factor γ calculated as the ratio of the SHG intensities parallel and perpendicular to the fiber axis (φ_0), which reflects the anisotropy of the nonlinear response of the protein,

$$\gamma = \sqrt{\frac{I(\varphi_0)}{I(\varphi_0 + 90°)}} \tag{A24}$$

(iv) the ratio of the two independent hyperpolarizability tensor components β_{zzz} and β_{zxx},

$$\frac{\beta_{zzz}}{\beta_{zxx}} \tag{A25}$$

(v) the deviation from cylindrical symmetry (DCS), which reflects how good the cylindrical hypothesis is on the distribution of SHG dipoles within the protein of interest,

$$\mathrm{DCS} = \frac{\sum_{\varphi=0}^{180} |\mathrm{I}(\varphi) - \mathrm{I}^{\mathrm{cyl}}(\varphi)|}{\max[\mathrm{I}(\varphi)]}. \tag{A26}$$

TABLE VI. Comparison of computed γ [Table I and Fig. 3(h)] and fitted γ.

Protein	DCS	$\gamma = \sqrt{\frac{I(\varphi_0)}{I(\varphi_0+90°)}}$	$\frac{\beta_{zzz}}{\beta_{zxx}}$	γ_{fit}	R^2
Collagen	0.07	1.40	1.41	1.397 ± 0.001	0.99
Myosin tail	0.800	0.44	0.49	0.438 ± 0.006	0.99
Tubulin dimer (GTP-tubulin)	4.33	1.48	3.70	3.72 ± 0.4	0.91
Microtubule GTP-tubulin)	0.01	2.49	2.49	2.489 ± 0.001	1
Actin	3.78	1.93	−3.9	3.57 ± 0.4	0.92

11. Evaluation of anisotropy factor γ from modeled pSHG profiles in different proteins

To further estimate the validity of the cylindrical symmetry, we fitted the modeled pSHG profiles with Eq. (A21) and for cylindrical symmetry and we obtained the values in Table VI. Proteins with cylindrical symmetry and low DCS show a good agreement between β_{zzz}/β_{zxx} and the γ fitted with cylindrical symmetry equation. Low DCS proteins fit present high R^2 values, while for high DCS proteins the goodness of the fit is lower.

12. Estimation of protein angular distribution and effective hyperpolarizability per peptide bonds with a simplified model

A simplified model, currently used in most of the literature [10,21,25,37,38], assumes cylindrical symmetry within the protein and the same polar angles ψ for all the SHG emitters. With this assumption it is possible to write the following expression,

$$\gamma = \frac{\beta_{zzz}}{\beta_{zxx}} = \frac{2}{\tan^2\psi}, \tag{A27}$$

and express the polar angle ψ of the SHG emitters as a function of the anisotropy factor γ,

$$\psi = \arctan\sqrt{\frac{2}{\gamma}}. \tag{A28}$$

We derived the polar angles ψ for the different proteins from the γ_β values computed with our model (Table I) and we obtained the values in Table VII. By comparing the polar angle ψ and the average angle of the PB distribution $\bar{\theta}_{zz'}$ we observed that they have the same value only in the case of collagen where the 3D distribution of the PBs is very narrow. For proteins such as myosin and tubulin the difference between ψ and $\bar{\theta}_{zz'}$ is larger and increases with the width of the angular dispersion of the peptide bonds distribution.

With the assumptions of the above described simplified model (SM) we can calculate the effective hyperpolarizability of a protein as follows:

$$\begin{aligned}\beta_{\text{protein}}^{\text{eff,SM}} &= \sqrt{\langle \text{I}^{\text{cyl}}(\varphi)\rangle} \\ &= \beta_{zxx}\sqrt{\langle \sin^2 2\varphi + (\sin^2\varphi + \gamma\cos^2\varphi)^2\rangle},\end{aligned} \tag{A29}$$

where the brackets denote the average on the angles φ. We obtain

$$\langle \sin^2 2\varphi + (\sin^2\varphi + \gamma\cos^2\varphi)^2\rangle = \frac{7}{8} + \frac{\gamma}{4} + \frac{3}{8}\gamma^2 \tag{A30}$$

and

$$\beta_{zxx} = \frac{1}{2}\cos\psi\sin^2\psi\beta_{z'z'z'}, \tag{A31}$$

with $\beta_{z'z'z'}$ the first hyperpolarizability of the PB.

By expressing ψ as a function of γ [Eq. (A28)] we can write the effective protein hyperpolarizability $\beta_{\text{protein}}^{\text{eff,SM}}$ as a function of the anisotropy factor γ and $\beta_{z'z'z'}$ as follows:

$$\begin{aligned}\beta_{\text{protein}}^{\text{eff,SM}} = \frac{1}{2}&\cos\left(\arctan\sqrt{\frac{2}{\gamma}}\right)\sin^2\left(\arctan\sqrt{\frac{2}{\gamma}}\right) \\ &\times\sqrt{\frac{7}{8}+\frac{\gamma}{4}+\frac{3}{8}\gamma^2}\,\beta_{z'z'z'}.\end{aligned} \tag{A32}$$

TABLE VII. Comparison of polar angle distribution and effective protein hyperpolarizability with the simplified model.

Protein	γ	$\psi = \arctan\sqrt{\frac{2}{\gamma}}$	$\bar{\theta}_{zz'}$	$\text{SD}(\theta_{zz'})$	$\beta_{\text{PB}}^{\text{eff,SM}}$	$\beta_{\text{PB}}^{\text{eff}}$
Collagen	1.41	50°	52°	9°	0.24	0.25
Myosin tail	0.49	63.4°	72°	12°	0.18	0.130
Microtubule (GTP-tubulin)	2.49	41.9°	83°	37°	0.27	0.044

TABLE VIII. Estimation of absolute values of the effective hyperpolarizability of proteins of known length.

Protein	Length (nm)	N_{PB}	β_{PB}^{eff}	$\beta_{protein}^{eff}$ (10^{-30} esu)	β^{expt} (10^{-30} esu)	Reference
Col1agen type I	290	3030	0.25	507	188	[43]
$[(\text{Pro-Pro-Gly})_{10}]_3$	8.6	87	0.25	14.6	14.9	[43]
GTP-tubulin dimer	10	851	0.056	32	190	[17]

Using the γ values computed with our model (Table I) we estimated the effective protein hyperpolarizability per peptide bond $\beta_{PB}^{eff,SM}$ with the simplified model,

$$\beta_{PB}^{eff,SM} = \frac{\beta_{protein}^{eff,SM}}{\beta_{z'z'z'}}, \tag{A33}$$

obtaining the values in Table VII.

We note that for collagen there is an excellent agreement between $\beta_{PB}^{eff,SM}$ calculated with the simplified model and the β_{PB}^{eff} calculated with our model because the angular distribution of the PBs in this protein is very narrow [Fig. 2(d)] and the calculated ψ is a good approximation of the average polar angle $\bar{\theta}_{zz'}$ (Tables I and VII). As the angular distribution of the harmonophores in the protein becomes broader in myosin and microtubules [Fig. 2(f) and Tables I and VII], the estimation of the effective protein susceptibility per PB with a simplified model $\beta_{PB}^{eff,SM}$ differs from the one provided by our molecular model that takes into account the actual distribution of the PBs inside the proteins. Therefore, the use of a simplified model in which the unique polar angle ψ is estimated, as often made in current literature, is valid for collagen, but it is incorrect for the other proteins with larger PB angular distribution because it does not have any physical meaning.

13. Estimation of absolute values of the effective hyperpolarizability of proteins of known length

We estimated the absolute values of the effective hyperpolarizability for three different proteins of known length (Table VIII) as follows:

$$\beta_{protein}^{eff} = \beta_{PB}^{eff} N_{PB} \beta_{z'z'z'}, \tag{A34}$$

where N_{PB} is the total number of PBs in the protein, β_{PB}^{eff} is the effective protein susceptibility per PB estimated for different proteins (Table I), and $\beta_{z'z'z'} = 0.67 \times 10^{-30}$ esu is the mean first hyperpolarizability of a PB estimated in Ref. [43].

We cannot directly compare the $\beta_{protein}^{eff}$ with the measured $\beta_{protein}^{HRS}$ in hyper-Rayleigh scattering experiments [17,43], because of different 3D orientational averaging coefficients. Still, our model predicts the right order of magnitude for $[(\text{Pro-Pro-Gly})_{10}]_3$ ($\beta^{HRS} = 14.9 \times 10^{-30}$ esu) [43]), as expected because this value is the one used to calculate $\beta_{z'z'z'}$ in Ref. [43]. The effective susceptibility of Col1agen type I might be overestimated ($\beta^{HRS} = 188 \times 10^{-30}$ esu) [43]) possibly because our model does not take into account the retardation of the exciting field and the harmonic field over the length of the protein of 290 nm [42]. On the other hand, our GTP-tubulin dimer effective hyperpolarizability appears to be underestimated compared to experimental measurements ($\beta^{HRS} = 190 \times 10^{-30}$ esu) [17] because in our model we are neglecting the aromatic amino acid contribution and a possible aggregation of dimers in solution.

[1] W. R. Zipfel, R. M. Williams, and W. W. Webb, *Nonlinear magic: Multiphoton microscopy in the biosciences*, Nat. Biotechnol. **21**, 1369 (2003).

[2] D. James and P. Campagnola, *Recent advancements in optical harmonic generation microscopy: Applications and perspectives*, BME Front. **2021**, 3973857 (2021).

[3] A. Aghigh, S. Bancelin, M. Rivard, M. Pinsard, H. Ibrahim, and F. Légaré, *Second harmonic generation microscopy: A powerful tool for bio-imaging*, Biophys. Rev. Lett. **15**, 43 (2023).

[4] P. Campagnola, A. Millard, M. Terasaki, P. Hoppe, C. Malone, and W. Mohler, *Three-dimensional high-resolution second-harmonic generation imaging of endogenous structural proteins in biological tissues*, Biophys. J. **82**, 493 (2002).

[5] A. Zoumi, A. Yeh, and B. Tromberg, *Imaging cells and extracellular matrix in vivo by using second-harmonic generation and two-photon excited fluorescence*, Proc. Natl. Acad. Sci. U.S.A. **99**, 11014 (2002).

[6] W. Zipfel, R. Williams, R. Christie, A. Nikitin, B. Hyman, and W. Webb, *Live tissue intrinsic emission microscopy using multiphoton-excited native fluorescence and second harmonic generation*, Proc. Natl. Acad. Sci. U.S.A. **100**, 7075 (2003).

[7] X. Chen, O. Nadiarynkh, S. Plotnikov, and P. Campagnola, *Second harmonic generation microscopy for quantitative analysis of collagen fibrillar structure*, Nat. Protoc. **7**, 654 (2012).

[8] S. Bancelin, C. Aimé, I. Gusachenko, L. Kowalczuk, G. Latour, T. Coradin, and M.-C. Schanne-Klein, *Determination of collagen fibril size via absolute measurements of second-harmonic generation signals*, Nat. Commun. **5**, 4920 (2014).

[9] T. Boulesteix, E. Beaurepaire, M. Sauviat, and M.-C. Schanne-Klein, *Second-harmonic microscopy of unstained living cardiac myocytes: measurements of sarcomere length with 20-nm accuracy*, Opt. Lett. **29**, 2031 (2004).

[10] S. Plotnikov, A. Millard, P. Campagnola, and W. Mohler, *Characterization of the myosin-based source for second-harmonic generation from muscle sarcomeres*, Biophys. J. **90**, 693 (2006).

[11] V. Nucciotti, C. Stringari, L. Sacconi, F. Vanzi, L. Fusi, M. Linari, G. Piazzesi, V. Lombardi, and F. Pavone, *Probing myosin structural conformation in vivo by second-harmonic generation microscopy*, Proc. Natl. Acad. Sci. U.S.A. **107**, 7763 (2010).

[12] D. Dombeck, K. Kasischke, H. Vishwasrao, M. Ingelsson, B. Hyman, and W. Webb, *Uniform polarity microtubule assemblies imaged in native brain tissue by second-harmonic generation microscopy*, Proc. Natl. Acad. Sci. U.S.A. **100**, 7081 (2003).

[13] W. Stoothoff, B. Bacskai, and B. Hyman, *Monitoring tau-tubulin interactions utilizing second harmonic generation in living neurons*, J. Biomed. Opt. **13**, 064039 (2008).

[14] N. Olivier, M. Luengo-Oroz, L. Duloquin, E. Faure, T. Savy, I. Veilleux, X. Solinas, D. Débarre, P. Bourgine, A. Santos, N. Peyriéras, and E. Beaurepaire, *Cell lineage reconstruction of early zebrafish embryos using label-free nonlinear microscopy*, Science **329**, 967 (2010).

[15] M. Didier, C. Macias-Romero, C. Teulon, P. Jourdain, and S. Roke, *Mapping of real-time morphological changes in the neuronal cytoskeleton with label-free wide-field second-harmonic imaging: A case study of nocodazole*, Neurophotonics **6**, 045006 (2019).

[16] S. Bancelin, C. Couture, M. Pinsard, M. Rivard, P. Drapeau, and F. Légaré, *Probing microtubules polarity in mitotic spindles in situ using interferometric second harmonic generation microscopy*, Sci. Rep. **7**, 6758 (2017).

[17] V. Van Steenbergen, W. Boesmans, Z. Li, Y. de Coene, K. Vints, P. Baatsen, I. Dewachter, M. Ameloot, K. Clays, and P. Vanden Berghe, *Molecular understanding of label-free second harmonic imaging of microtubules*, Nat. Commun. **10**, 3530 (2019).

[18] A. Kwan, K. Duff, G. Gouras, and W. Webb, *Optical visualization of Alzheimers pathology via multiphoton-excited intrinsic fluorescence and second harmonic generation*, Opt. Express **17**, 3679 (2009).

[19] S. Wang, B. Lin, G. Lin, C. Sun, R. Lin, J. Huang, J. Tao, X. Wang, Y. Wu, L. Chen, and J. Chen, *Label-free multiphoton imaging of β-amyloid plaques in Alzheimer's disease mouse models*, Neurophotonics **6**, 045008 (2019).

[20] P. Stoller, K. Reiser, P. Celliers, and A. Rubenchik, *Polarization-modulated second harmonic generation in collagen*, Biophys. J. **82**, 3330-42 (2002).

[21] F. Tiaho, G. Recher, and D. Rouède, *Estimation of helical angles of myosin and collagen by second harmonic generation imaging microscopy*, Opt. Express **15**, 12286 (2007).

[22] P. Su, W. Chen, Y. Chen, and C. Dong, *Determination of collagen nanostructure from second-order susceptibility tensor analysis*, Biophys. J. **100**, 2053 (2011).

[23] J. Duboisset, D. Ait-Belkacem, M. Roche, H. Rigneault, and S. Brasselet, *Generic model of the molecular orientational distribution probed by polarization-resolved second-harmonic generation*, Phys. Rev. A **85**, 043829 (2012).

[24] G. Latour, I. Gusachenko, L. Kowalczuk, I. Lamarre, and M.-C. Schanne-Klein, *In vivo structural imaging of the cornea by polarization-resolved second harmonic microscopy*, Biomed. Opt. Express **3**, 1 (2012).

[25] I. Gusachenko, V. Tran, Y. Goulam Houssen, J.-M. Allain, and M.-C. Schanne-Klein, *Polarization-resolved second-harmonic generation in tendon upon mechanical stretching*, Biophys. J. **102**, 2220 (2012).

[26] A. Tuer, M. Akens, S. Krouglov, D. Sandkuijl, B. Wilson, C. Whyne, and V. Barzda, *Hierarchical model of fibrillar collagen organization for interpreting the second-order susceptibility tensors in biological tissue*, Biophys. J. **103**, 2093 (2012).

[27] R. Cicchi, N. Vogler, D. Kapsokalyvas, B. Dietzek, J. Popp, and F. Pavone, *From molecular structure to tissue architecture: Collagen organization probed by SHG microscopy*, J. Biophoton. **6**, 129 (2013).

[28] M. Samim, N. Prent, D. Dicenzo, B. Stewart, and V. Barzda, *Second harmonic generation polarization properties of myofilaments*, J. Biomed. Opt. **19**, 056005 (2014).

[29] C. Yu, N. Langowitz, H. Wu, R. Farhadifar, J. Brugues, T. Yoo, and D. Needleman, *Measuring microtubule polarity in spindles with second-harmonic generation*, Biophys. J. **106**, 1578 (2014).

[30] A. Golaraei, L. Kontenis, R. Cisek, D. Tokarz, S. Done, B. Wilson, and V. Barzda, *Changes of collagen ultrastructure in breast cancer tissue determined by second-harmonic generation double Stokes-Mueller polarimetric microscopy*, Biomed. Opt. Express **7**, 4054 (2016).

[31] K. Campbell, R. Chaudhary, J. Handel, M. Patankar, and P. Campagnola, *Polarization-resolved second harmonic generation imaging of human ovarian cancer*, J. Biomed. Opt. **23**, 1 (2018).

[32] P. Johnson, A. Karvounis, H. Singh, C. Brereton, K. Bourdakos, K. Lunn, J. Roberts, D. Davies, O. Muskens, M. Jones, and S. Mahajan, *Superresolved polarization-enhanced second-harmonic generation for direct imaging of nanoscale changes in collagen architecture*, Optica **8**, 674 (2021).

[33] S. Stanciu, R. Hristu, G. Stanciu, D. Tranca, L. Eftimie, A. Dumitru, M. Costache, H. Stenmark, H. Manders, A. Cherian, M. Tark-Dame, and E. Manders, *Super-resolution re-scan second harmonic generation microscopy*, Proc. Natl. Acad. Sci. U.S.A. **119**, e2214662119 (2022).

[34] S. Psilodimitrakopoulos, D. Artigas, G. Soria, I. Amat-Roldan, A. Planas, and P. Loza-Alvarez, *Quantitative discrimination between endogenous SHG sources in mammalian tissue, based on their polarization response*, Opt. Express **17**, 10168 (2009).

[35] D. Sharoukhov and H. Lim, *On probing conformation of microtubules by second-harmonic generation*, J. Mod. Opt. **63**, 71 (2016).

[36] H. Fujita, J. Kaneshiro, M. Takeda, K. Sasaki, R. Yamamoto, D. Umetsu, E. Kuranaga, S. Higo, T. Kondo, Y. Asano, Y. Sakata, S. Miyagawa, and T. Watanabe, *Estimation of crossbridge-state during cardiomyocyte beating using second harmonic generation*, Life Sci. Alliance **6**, e202302070 (2023).

[37] S. Psilodimitrakopoulos, V. Petegnief, N. de Vera, O. Hernandez, D. Artigas, A. Planas, and P. Loza-Alvarez, *Quantitative imaging of microtubule alteration as an early*

marker of axonal degeneration after ischemia in neurons, Biophys. J. **104**, 968 (2013).
[38] J. Kaneshiro, Y. Okada, T. Shima, M. Tsujii, K. Imada, T. Ichimura, and T. Watanabe, *Second harmonic generation polarization microscopy as a tool for protein structure analysis*, Biophys. Physicobiol. **16**, 147 (2019).
[39] T. Shima, M. Morikawa, J. Kaneshiro, T. Kambara, S. Kamimura, T. Yagi, H. Iwamoto, S. Uemura, H. Shigematsu, M. Shirouzu, T. Ichimura, T. Watanabe, R. Nitta, Y. Okada, and N. Hirokawa, *Kinesin-binding-triggered conformation switching of microtubules contributes to polarized transport*, J. Cell Biol. **217**, 4164 (2018).
[40] S. Mitchell, R. McAloney, D. Moffatt, N. Mora-Diez, and M. Zgierskij, *Second-harmonic generation optical activity of a polypeptide alpha-helix at the air/water interface*, J. Chem. Phys. **122**, 114707 (2005).
[41] J. M. Perry, A. J. Moad, N. J. Begue, R. D. Wampler, and G. J. Simpson, *Electronic and vibrational second-order nonlinear optical properties of protein secondary structural motifs*, J. Phys. Chem. B **109**, 20009 (2005).
[42] A. Deniset-Besseau, J. Duboisset, E. Benichou, F. Hache, P.-F. Brevet, and M.-C. Schanne-Klein, *Measurement of the second-order hyperpolarizability of the collagen triple helix and determination of its physical origin*, J. Phys. Chem. B **113**, 13437 (2009).
[43] J. Duboisset, A. Deniset-Besseau, E. Benichou, I. Russier-Antoine, N. Lascoux, C. Jonin, F. Hache, M.-C. Schanne-Klein, and P.-F. Brevet, *A bottom-up approach to build the hyperpolarizability of peptides and proteins from their amino acids*, J. Phys. Chem. B **117**, 9877 (2013).
[44] *Protein Data Bank*, https://www.rcsb.org/.
[45] D. Débarre, N. Olivier, W. Supatto, and E. Beaurepaire, *Mitigating phototoxicity during multiphoton microscopy of live drosophila embryos in the 1.0-1.2 m wavelength range*, PLoS One **9**, e104250 (2014).
[46] I. Durn, M. Mar-Beffa, J. Santamara, J. Becerra, and L. Santos-Ruiz, *Actinotrichia collagens and their role in fin formation*, Dev. Biol. **354**, 160 (2011).
[47] See Supplemental Material at http://link.aps.org/supplemental/10.1103/PhysRevX.14.011038 for comparison of the model with other theoretical approaches, additional calculation on the implication of plane wave assumption and supplemental data (8 figures, 2 tables, and 14 videos).
[48] https://github.com/skielex/structure-tensor.
[49] P. Réfrégier, M. Roche, and S. Brasselet, *Precision analysis in polarization-resolved second harmonic generation microscopy*, Opt. Lett. **36**, 2149 (2011).
[50] C. Teulon, I. Gusachenko, G. Latour, and M. Schanne-Klein, *Theoretical, numerical and experimental study of geometrical parameters that affect anisotropy measurements in polarization-resolved SHG microscopy*, Opt. Express **23**, 9313 (2015).
[51] A. Tuer, S. Krouglov, N. Prent, R. Cisek, D. Sandkuijl, K. Yasufuku, B. Wilson, and V. Barzda, *Nonlinear optical properties of type I collagen fibers studied by polarization dependent second harmonic generation microscopy*, J. Phys. Chem. B **115**, 12759 (2011).
[52] M. de Wergifosse, J. de Ruyck, and B. Champagne, *How the second-order nonlinear optical response of the collagen triple helix appears: A theoretical investigation*, J. Phys. Chem. C **118**, 8595 (2014).
[53] X. Dow, E. DeWalt, S. Sullivan, P. Schmitt, J. Ulcickas, and G. Simpson, *Imaging the nonlinear susceptibility tensor of collagen by nonlinear optical Stokes ellipsometry*, Biophys. J. **111**, 1361 (2016).
[54] S. J. Lalama and A. F. Garito, *Origin of the nonlinear second-order optical susceptibilities of organic systems*, Phys. Rev. A **20**, 1179 (1979).
[55] I. Rocha-Mendoza, D. Yankelevich, M. Wang, K. Reiser, C. Frank, and A. Knoesen, *Sum frequency vibrational spectroscopy: The molecular origins of the optical second-order nonlinearity of collagen*, Biophys. J. **93**, 4433 (2007).
[56] R. Berisio, L. Vitagliano, L. Mazzarella, and A. Zagari, *Crystal structure of the collagen triple helix model* $[(\text{Pro-Pro-Gly})_{10}]_3$, Protein Sci. **11**, 262 (2002).
[57] W. Blankenfeldt, N. Thoma, J. Wray, M. Gautel, and I. Schlichting, *Crystal structures of human cardiac β-myosin II S2-Δ provide insight into the functional role of the S2 subfragment*, Proc. Natl. Acad. Sci. U.S.A. **103**, 17713 (2006).
[58] G. Alushin, G. Lander, E. Kellogg, R. Zhang, D. Baker, and E. Nogales, *High-resolution microtubule structures reveal the structural transitions in αβ-tubulin upon GTP hydrolysis*, Cell **157**, 1117 (2014).
[59] P. Gurel, L. Kim, P. Ruijgrok, T. Omabegho, Z. Bryant, and G. Alushin, *Cryo-EM structures reveal specialization at the myosin VI-actin interface and a mechanism of force sensitivity*, eLife **6**, e31125 (2017).
[60] C. Loison and D. Simon, *Additive model for the second harmonic generation hyperpolarizability applied to a collagen-mimicking peptide* $(\text{Pro-Pro-Gly})_{10}$, J. Phys. Chem. A **114**, 7769 (2010).
[61] J. Duboisset, G. Matar, I. Russier-Antoine, E. Benichou, G. Bachelier, C. Jonin, D. Ficheux, F. Besson, and P.-F. Brevet, *First hyperpolarizability of the natural aromatic amino acids tryptophan, tyrosine, and phenylalanine and the tripeptide lysine-tryptophan-lysine determined by hyper-Rayleigh scattering*, J. Phys. Chem. B **114**, 13861 (2010).
[62] J. Guthmuller and D. Simon, *Linear and nonlinear optical response of aromatic amino acids: A time-dependent density functional investigation*, J. Phys. Chem. A **110**, 9967 (2006).
[63] I. Gusachenko and M.-C. Schanne-Klein, *Numerical simulation of polarization-resolved second-harmonic microscopy in birefringent media*, Phys. Rev. A **88**, 053811 (2013).
[64] I. Gusachenko, G. Latour, and M.-C. Schanne-Klein, *Polarization-resolved second harmonic microscopy in anisotropic thick tissues*, Opt. Express **18**, 19339 (2010).
[65] M. Samim, S. Krouglov, and V. Barzda, *Double Stokes Mueller polarimetry of second-harmonic generation in ordered molecular structures*, J. Opt. Soc. Am. B **32**, 451 (2015).
[66] K. Fung, M. Samim, A. Gribble, V. Barzda, and I. Vitkin, *Monte Carlo simulation of polarization-sensitive second-harmonic generation and propagation in biological tissue*, J. Biophoton. **11**, e201800036 (2018).
[67] F. Vanzi, M. Capitanio, L. Sacconi, C. Stringari, R. Cicchi, M. Canepari, M. Maffei, N. Piroddi, C. Poggesi, V. Nucciotti, M. Linari, G. Piazzesi, C. Tesi, R. Antolini, V. Lombardi, R. Bottinelli, and F. Pavone, *New techniques in*

linear and non-linear laser optics in muscle research, J. Muscle Res. Cell Motil. **27**, 469 (2006).

[68] A. J. Moad, C. W. Moad, J. M. Perry, R. D. Wampler, J. Begue, N, T. Shen, G. S. Goeken, R. Heiland, and G. J. Simpson, *NLOPREDICT: Visualization and data analysis software for nonlinear optics*, J. Comput. Chem. **28**, 1996 (2007).

[69] M. Schmeltz, C. Teulon, G. Latour, D. Ghoubay, V. Borderie, C. Aimé, and M. Schanne-Klein, *Implementation of artifact-free circular dichroism SHG imaging of collagen*, Opt. Express **27**, 22685 (2019).

[70] H. Goodson and E. Jonasson, *Microtubules and microtubule-associated proteins*, Cold Spring Harb. Perspect Biol. **10**, a022608 (2018).

[71] L. Kontenis, M. Samim, A. Karunendiran, S. Krouglov, B. Stewart, and V. Barzda, *Second harmonic generation double Stokes Mueller polarimetric microscopy of myofilaments*, Biomed. Opt. Express **7**, 559 (2016).

[72] C. Teulon, A. Tidu, F. Portier, G. Mosser, and M.-C. Schanne-Klein, *Probing the 3D structure of cornea-like collagen liquid crystals with polarization-resolved SHG microscopy*, Opt. Express **24**, 16084 (2016).

[73] A. C. Kwan, D. A. Dombeck, and W. W. Webb, *Polarized microtubule arrays in apical dendrites and axons*, Proc. Natl. Acad. Sci. U.S.A. **105**, 11370 (2008).

[74] J. Howard and A. Hyman, *Dynamics and mechanics of the microtubule plus end*, Nature (London) **422**, 753 (2003).

[75] A. Yvon, P. Wadsworth, and M. Jordan, *Taxol suppresses dynamics of individual microtubules in living human tumor cells*, Mol. Biol. Cell **10**, 947 (1999).

[76] E. Mukhtar, V. Adhami, and H. Mukhtar, *Targeting microtubules by natural agents for cancer therapy*, Nature (London) **13**, 275 (2014).

[77] K. R. Brunden, V. M.-Y. Lee, A. M. B. Smith III, J. Q. Trojanowski, and C. Ballatore, *Altered microtubule dynamics in neurodegenerative disease: Therapeutic potential of microtubule-stabilizing drugs*, Neurobiology of disease **105**, 328 (2017).

[78] J. Sleigh, A. Rossor, A. Fellows, A. Tosolini, and G. Schiavo, *Axonal transport and neurological disease*, Nat. Rev. Neurol. **15**, 691 (2019).

[79] J. Wei, J.-Y. Wang, M.-Y. Zhang, G.-L. Chai, C.-S. Lin, and W.-D. Cheng, *Single amino acid mutation in alpha-helical peptide affect second harmonic generation hyperpolarizability*, Chem. Phys. Lett. **556**, 260 (2013).

[80] A. Duan, E. M. Jonasson, E. Alberico, C. Li, R. Scripture, J. P. Miller, M. Alber, and H. Goodson, *Interactions between tau and different conformations of tubulin: Implications for tau function and mechanism*, Chem. Phys. Lett. **429**, 1424 (2017).

[81] E. Kellogg, N. Hejab, S. Poepsel, K. Downing, F. DiMaio, and E. Nogales, *Near-atomic model of microtubule-tau interactions*, Science **360**, 1242 (2018).

[82] J. Hervy and D. Bicout, *Dynamical decoration of stabilized-microtubules by tau-proteins*, Sci. Rep. **9**, 12473 (2019).

[83] P. Baas and L. Qiang, *Tau: It's not what you think*, Trends Cell Biol. **29**, 452 (2019).

[84] J. Jumper *et al.*, *Highly accurate protein structure prediction with alphafold*, Nature (London) **596**, 583 (2021).

[85] M. Baek *et al.*, *Accurate prediction of protein structures and interactions using a three-track neural network*, Science **373**, 871 (2021).

[86] V. Marx, *Method of the year: Protein structure prediction*, Nat. Methods **19**, 5 (2022).

[87] P. Johansson and P. Koelsch, *Label-free imaging of amyloids using their intrinsic linear and nonlinear optical properties*, Biomed. Opt. Express **8**, 743 (2017).

[88] C. Dobson, T. Knowles, and M. Vendruscolo, *The amyloid phenomenon and its significance in biology and medicine*, Cold Spring Harbor Perspect. Biol. **12**, a033878 (2020).

[89] P. Ke, R. Zhou, L. Serpell, R. Riek, T. Knowles, H. Lashuel, E. Gazit, I. Hamley, T. Davis, M. Fndrich, D. Otzen, M. Chapman, C. Dobson, D. Eisenberg, and R. Mezzenga, *Half a century of amyloids: Past, present and future*, Chem. Soc. Rev. **49**, 5473 (2020).

[90] W. Rice, S. Firdous, S. Gupta, M. Hunter, C. Foo, Y. Wang, H. Kim, D. Kaplan, and I. Georgakoudi, *Non-invasive characterization of structure and morphology of silk fibroin biomaterials using non-linear microscopy*, Biomaterials **29**, 2015 (2008).

[91] Y. Shen, A. Levin, A. Kamada, Z. Toprakcioglu, M. Rodriguez-Garcia, Y. Xu, and T. Knowles, *From protein building blocks to functional materials*, ACS Nano **15**, 5819 (2021).

[92] B. Asadipour, E. Beaurepaire, X. Zhang, A. Chessel, P. Mahou, W. Supatto, M.-C. Schanne-Klein, and C. Stringari, *Modelling and predicting second harmonic generation from protein molecular structure*, Zenodo (2023), 10.5281/zenodo.10410596.

[93] J. Schindelin, I. Arganda-Carreras, E. Frise, V. Kaynig, M. Longair, T. Pietzsch, S. Preibisch, C. Rueden, S. Saalfeld, B. Schmid *et al.*, *Fiji: An open-source platform for biological-image analysis*, Nat. Methods **9**, 676 (2012).

[94] J. Bigun and G. Granlund, *Optimal orientation detection of linear symmetry*, in *Proceedings of the IEEE First International Conference on Computer Vision, 2006* (IEEE Computer Society Press, 1987), pp. 433–438.

[95] T. E. A. Brox, *Adaptive structure tensors and their applications*, in *Visualization and Processing of Tensor Fields. Mathematics and Visualization*, edited by J. Weickert and H. Hagen (Springer, New York, 2006).

[96] G. Ducourthial, J. Affagard, M. Schmeltz, X. Solinas, M. Lopez-Poncelas, C. Bonod-Bidaud, R. Rubio-Amador, F. Ruggiero, J. Allain, E. Beaurepaire, and M. C. Schanne-Klein, *Monitoring dynamic collagen reorganization during skin stretching with fast polarization-resolved second harmonic generation imaging*, J. Biophoton. **12**, e201800336 (2019).

[97] R. Boyd, *Nonlinear Optics* (Academic Press, New York, 2003).

[98] D. Kleinmann, *Theory of second harmonic generation of light*, Phys. Rev. **128**, 1761 (1962).